Investigation of the Au-induced morphology of 3.8 and 12.3 degree silicon surfaces

by

Wei Wu

A thesis submitted in partial fulfillment of the requirements
for the degree of Master of Science
Department of Physics
Lakehead University

Your file Votre référence
ISBN: 978-0-494-33585-7
Our file Notre référence
ISBN: 978-0-494-33585-7

ABSTRACT

We have used a combination of scanning tunneling microscopy (STM) and low energy electron diffraction to investigate the Au-induced morphology of vicinal Si samples miscut from (111) by 3.8°, and 12.3° toward $[11\bar{2}]$. The surface morphology changes dramatically with Au coverage on both samples. On the 3.8° samples, gold deposition leads to the formation of the (775) facets. The (775) facet is orientated 8.5° toward $[11\bar{2}]$ and characterized by 1-d chains running along $[1\bar{1}0]$ with a spacing of 21.3 $\mathring{A}$. The formation of the (775) facet is consistent with previous ideas that it represents a low energy facet on these surfaces. On the 12.3° sample no single low energy facet was observed in the coverage range (0-0.24ML) investigated. Instead, (13 13 7), (995), and (553) facets are formed at 0.10 ML, 0.20 ML, and 0.24 ML respectively.

Chapter 1: Introduction 3

Chapter 2: Background 5

2.1 Silicon crystallography 5

2.2 Gold Induced Surface Restructuring 9

2.2.1 Gold induced restructuring on flat surfaces 9

2.2.2 Gold induced restructuring on vicinal surface 11

Chapter 3: Experimental Techniques 17

3.1 Instrumentation 17

3.1.1. UHV system 17

3.1.2 Low Energy Electron Diffraction 20

3.1.3 Auger Electron Spectroscopy 24

3.1.4 Scanning Tunneling Microscopy 28

3.1.4.1 Quantum Theory of Tunneling 28

3.1.4.2 Tip Preparation and STM Instrumentation 30

3.2 Sample Preparation 33

3.2.1 Clean surface preparation 33

3.2.2. Au evaporator 35

Chapter 4: Results 37

4.1 Morphology of 3.8° samples as function of Au coverage 37

4.2 Morphology of 12.3° samples 47

Chapter 5: Discussion 55

Chapter 6: Conclusion 59

References 61

Chapter 1: Introduction

One dimensional (1-d) nanostructured materials have attracted a great deal of scientific interest. They provide potential for understanding both fundamental physical concepts, and for applications in nanoscale electronic and optoelectronic devices and bio-sensing techniques[1,2]. One of the recent areas of investigation is the self-assembly of Au-induced atomic wires on Silicon surfaces. It is thought that these systems may act as prototypical systems to study the 1-d confinement of electrons[3-7].

Electronic behaviour becomes more exotic as the dimensions of the system are reduced[8]. Single particle excitations are replaced by collective excitations. The electronic and structural properties of 1-d metallic systems are predicted to be fundamentally different from those in higher dimensions.[9] In particular, in the Luttinger liquid[10] (a quantum liquid in one dimension), it is proposed that the collective excitations associated with charge and spin separate to form holons and spinons respectively.

It is well known that 1-d metals are prone to a variety of structural and electronic instabilities. For example, many systems are prone to a Peierls distortion[11] where a doubling of the unit cell leads to a metal-insulator transition. In other words metalicity collapses in one dimension unless there are interaction potentials stabilizing it. One way to avoid this transition may be to deposit the 1-d atomic chains on a rigid template.[3]

Vicinal, or miscut, silicon surfaces are attractive substrates for the formation of 1-d wires.[9] Vicinal surfaces can be prepared with regular step arrays, and the

bulk band gap prevents hybridization of the chain states at the surface with the bulk.

Previously, J.N.Crain et al.[12] have demonstrated that a variety of chain structures with novel 1-d behaviour can be prepared by evaporating a small amount of gold onto vicinal silicon substrates. They show that the dimensionality of these chains can be tailored by varying the gold coverage and the angle of the miscut.

Much of the work to date has focused on the electronic properties of the chains; while relatively little work has investigated their formation. In this thesis we expand upon previous experiments and study the Au-induced morphology of wafers orientated 3.8° and 12.3° away from the (111) plane towards $[11\bar{2}]$. On the 3.8° wafer, we vary the gold coverage from 0-0.46 monolayers (ML), and on the 12.3° sample we study coverages ≤ 0.24 ML.

In Chapter 2 we develop the necessary background and review previous results. In Chapter 3 we discuss the experimental techniques and sample preparation. Our results are presented in Chapter 4 and are discussed in Chapter 5. Chapter 6 gives a brief summary of our findings.

Chapter 2: Background

2.1 Silicon crystallography

The crystal structure of silicon is a diamond lattice. It consists of tetrahedral bonds. As seen in Figure 2-1-1, each atom has 4 nearest neighbors and 12 next nearest neighbors. The space lattice of silicon is a face-center-cubic (fcc) structure, with a two atom basis, one at (000), and the second offset at $(\frac{1}{4}, \frac{1}{4}, \frac{1}{4},)$.

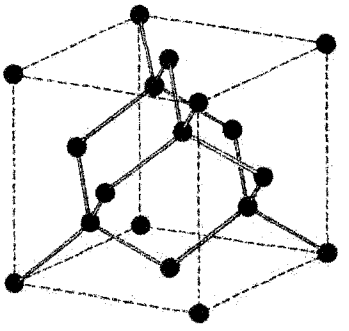

Figure 2-1-1 crystal structure of silicon, showing the tetrahedral bond arrangement. Figure reproduced from Reference 13.

The natural cleavage plane of Silicon is the (111) plane where (111) is the Miller-index. The Miller-index of a surface is defined in Figure 2-1-2. All the surfaces referred to in this thesis are labeled in the same way.

The bulk terminated (111) surface exhibits hexagonal symmetry with a lattice spacing of $3.8\,\mathring{A}$. For many surfaces, to reduce the number of dangling bonds atoms rearrange themselves from their bulk terminated positions to reduce the overall surface energy. This rearrangement is called surface reconstruction.

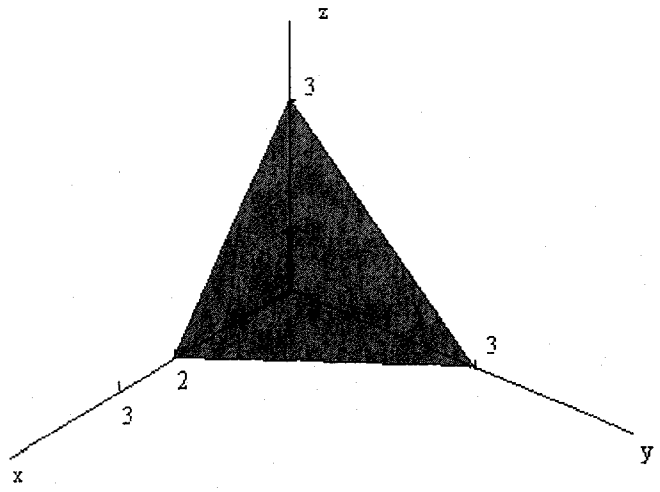

Figure 2-1-2 The intercept of a plane with the crystal axes is 2a, 3b, and 3c respectively. The reciprocals of the intercepts are $\frac{1}{2}$, $\frac{1}{3}$, and $\frac{1}{3}$. The smallest three integers having the same ratio is 3, 2, and 2, thus this plane is defined as the (322) plane. Figure reproduced from Reference 13.

The 7x7 structure is the low energy reconstruction for the clean Si(111) surface below 850° C. The 7x7 unit cell (with a unit length of 26.6 $\mathring{A}$) is 7 times larger than the bulk terminated unit cell. The surface unit cell in real space retains the same hexagonal symmetry. The accepted model for the 7x7 reconstruction was proposed by Takayanagi et al.[14] and is called the dimer adatom stacking fault (DAS) model (Figure 2-1-3). The key structural features of this model are: (a) 12 "adatoms" in the top layer, (b) a stacking fault in one of the two triangular subunits of the second layer, (c) nine dimers that border the triangular subunits in the third layer, and (d) a vacancy at each apex of the unit cell, the so called corner holes.

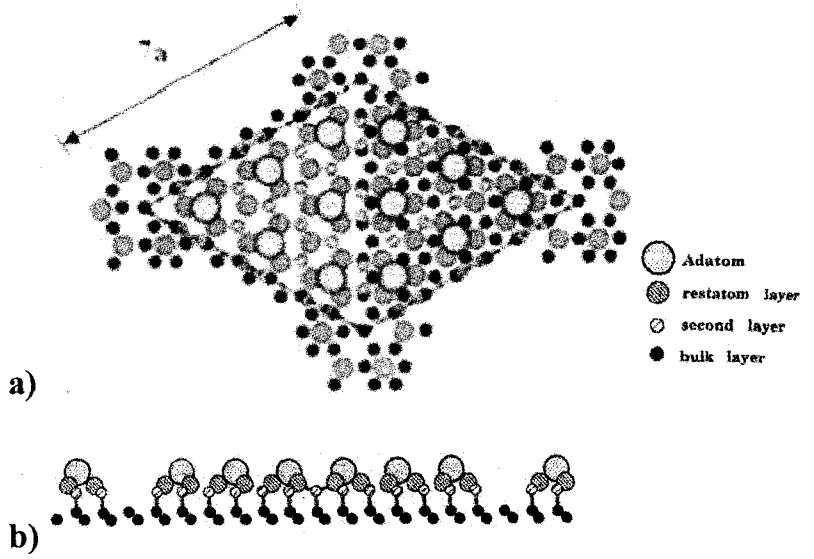

Figure 2-1-3 DAS model of Si (111)-7x7: (a) first three layers of atoms shown in top view. The surface unit cell is outlined (Robinson et al., 1986) Figure reproduced from Reference 16. (b) side view of the 7x7 reconstructions. Figure reproduced from Reference 15.

In Figure 2-1-4, we show an STM image of the 7x7 reconstruction. We can clearly see each half of the 7x7 unit cell, and the boundary between each triangular subunit. In fact, the first STM observation of the 7x7 reconstruction by Binnig et al.[16] in 1981 was instrumental in verifying the 7x7 DAS model and the subsequent award of a Nobel Prize in 1986 to Binnig and Rohrer.

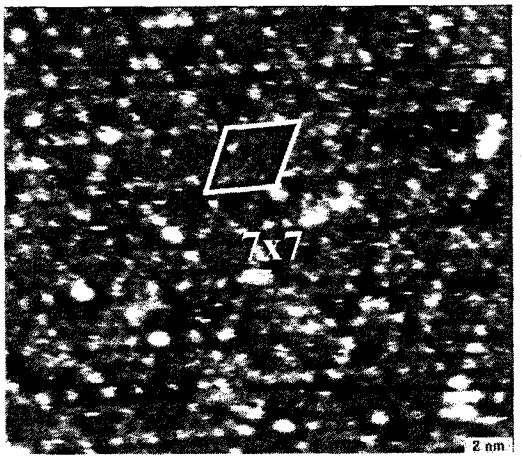

Figure 2-1-4 An STM image (160 Å ×200 Å) of a clean 3.8° sample. The image was taken at a bias of +2.14 V, a tunneling current of 0.53 nA, with a PtRh tip.

Besides the natural cleavage plane, silicon can be intentionally cut along any direction. Wafers cut away from the (111) plane are referred to as "vicinal surfaces". Vicinal wafers tilted towards $[11\bar{2}]$ or $[\bar{1}\bar{1}2]$ are particularly interesting since they exploit the crystallography of the Si crystal to produce well defined atomic steps running straight along the $\{1\bar{1}0\}$ directions. The two directions exhibit very different behavior. Unreconstructed Si atoms at the step edge in the $[11\bar{2}]$ direction have one dangling bond per atom while atoms at the edge of $[\bar{1}\bar{1}2]$ steps have two (Figure 2-1-5). In this thesis I will focus on vicinal wafers orientated towards $[11\bar{2}]$.

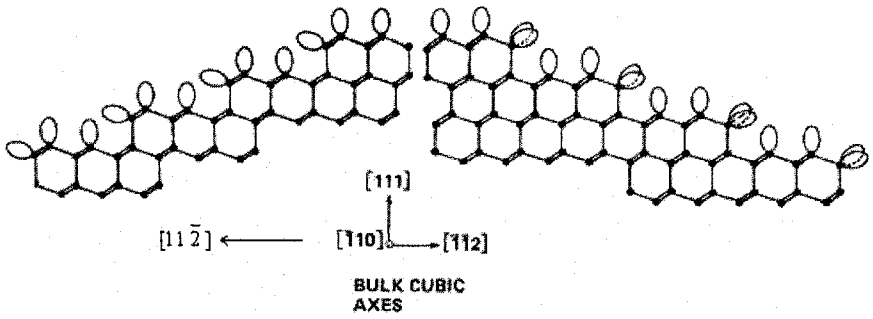

Figure 2-1-5 Diagram of steps cut along $[\bar{1}\bar{1}2]$ and $[11\bar{2}]$. Figure reproduced from Reference 17.

Cleavage produces atomic steps which can form facets. The morphology of vicinal crystal surfaces is mainly determined by the distribution of atomic steps. This distribution depends on miscut angle, sample preparation[18,19], and metal coverage[20].

In this thesis we employ a heating procedure outlined by L.Lin et al.[21]. Figure 2-1-6 shows two examples of the morphology of the clean 3.8° and 12.3° surfaces following heat treatment. It is clear from the STM images that even though the two wafers are miscut towards $[11\bar{2}]$, the clean surfaces are quite different. The surfaces are far from flat. The clean 3.8° exhibits large (111)

terraces separated by facets tilted 7° away from the (111) plane. The 12.3° surface forms smaller terraces characterized by regular chain structures running along [1$\bar{1}$0] separated by atomic steps. Further details of this morphology will be discussed in chapter 4.

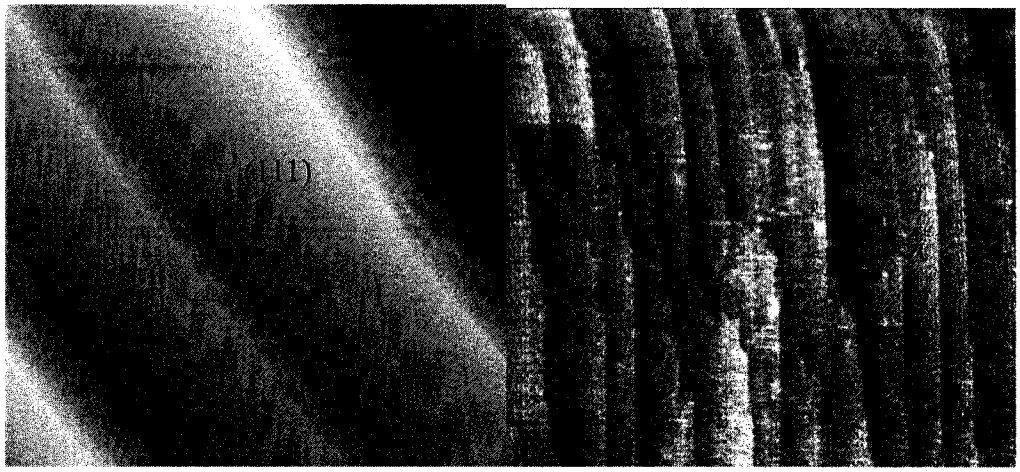

Figure 2-1-6 (a) An STM image (2000 Å × 1800 Å) of a 3.8° clean surface taken at a bias of +2.32 V, tunneling current of 29.0 pA, with a PtRh tip. (b) An STM image (3000 Å × 3000 Å) of a clean 12.3° surface taken at a bias of +2.42 V, tunneling current of 323 pA, with a PtRh tip.

2.2 Gold Induced Surface Restructuring

2.2.1 Gold induced restructuring on flat surfaces

For Si(111) surfaces, upon Au adsorption, the 7x7 reconstruction transforms into a 5x2 reconstruction. Normally this reconstruction occurs on flat (111) terraces but it also persists on samples with slight miscut[22 – 24]. According to measurements by Bauer, et al.[25,26], the Au coverage for the (5x2) is 0.443±0.008 ML, where one monolayer is defined by the density of Si(111) surface atoms and is equivalent to 7.8×10^{14} *atoms/cm*^{2}. This experimental value implies an average of 2 Au atoms per 5x2 unit cell.

Although the exact structure of this surface is still under debate, the model

displayed in Figure 2-2-1 was recently proposed by Steven C. Erwin[27]. The reconstruction occurs purely in the surface layer, and includes a double honeycomb chain (DHC) structure with an underlying 5x2 periodicity. Honeycomb chains occur when Si atoms are bonded to three atoms in the same layer but not to a fourth in the layer below. One chain is formed by hexagons of alternating Au and Si atoms while the other one consists of pure Si atoms. The gold atoms sit within the outermost Si double layer[28,29]. LEED patterns of the 5x2 reconstruction exhibit half order streaks between two rows running along $[11\bar{2}]$. The streaks are the result of incoherence of the 2x periodicity between two adjacent rows.

An STM image of 5x2 reconstruction is shown in Figure 2-2-2. The unit cell of 5x2 reconstruction is shown in white. The 2x periodicity is running along the chains in the $[1\bar{1}0]$ direction. The bright protrusions evident along the chains are extra silicon adatoms and they are located randomly. The extra adatoms occupy 1/4 of the available 5x2 sites. In fact they randomly populate about one half of the sites on a 5x4 superlattice. It has been proposed that the presence of these adatoms is the key to the electronic stability of the 5x2 structure[27].

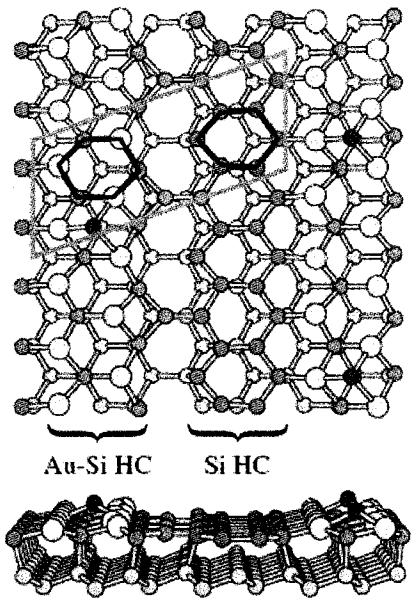

Figure 2-2-1"Double honeycomb chain" structure of Si (111)-(5x2)-Au. Large yellow circles are Au, small circles are Si. The elementary 5x2 unit cell is outlined. Each unit cell contains two honeycomb chains (HC) based on the outlined hexagons, one of alternating Au and Si atoms, the other of all Si. Three additional Si adatoms, in dark colour, are also shown. The origin of the adatoms is discussed in the text. Figure reproduced from Reference 27.

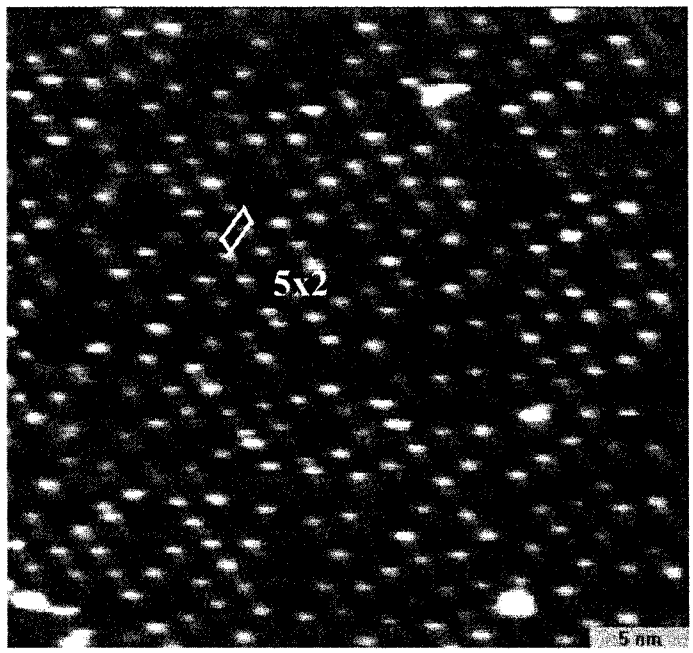

Figure 2-2-2 An STM image (320 $\mathring{A}$ × 210 $\mathring{A}$) taken on a 3.8° sample following 0.44±0.03 ML of gold. The image was taken at a bias of -2.45 V, a tunneling current of 420 pA, with a tungsten tip. A 5x2 unit cell is outlined.

2.2.2 Gold induced restructuring on vicinal surface

When gold is introduced onto vicinal surfaces, as we will see, it dramatically affects the morphology of the surface. The exact nature of the restructuring depends on Au coverage, deposition conditions and the wafer orientation. Au adsorption often produces well defined facets not observed on the clean surface to decrease the total surface energy.

D.J.Chadi[17] showed that for wafers orientated towards $[11\bar{2}]$, the relationship between the surface normal (relative to the bulk cubic axes) and the Miller-index is given by:

$$\vec{n} = (p+m,\ p+m,\ p-m),\ p \geq m \geq 1 \qquad (2.1)$$

$$\tan\theta = \frac{2m\sqrt{2}}{3p+m} \qquad (2.2)$$

$$d = (p+m/3)\,a \qquad (2.3)$$

where m is the number of atomic layers missing between two adjacent terraces. For the 3.8° wafer, m always equals 1. The angle θ is between the unknown facet and the (111) plane and p is the number of bulk atoms across the terrace. Assuming the facet consists of (111) terraces separated by atomic steps, Equation 2.3 yields the periodicity of the structure along the $[11\bar{2}]$ direction.

Figure 2-2-3 illustrates a vertical cut through a bulk silicon crystal. The [111] direction is vertical and $[1\bar{1}0]$ is into the page. In the figure, if you connect the leftmost point to any other point, this defines the labeled facet with respect to the (111) plane. The red and blue lines represent the orientation of our 3.8° and 12.3° samples respectively.

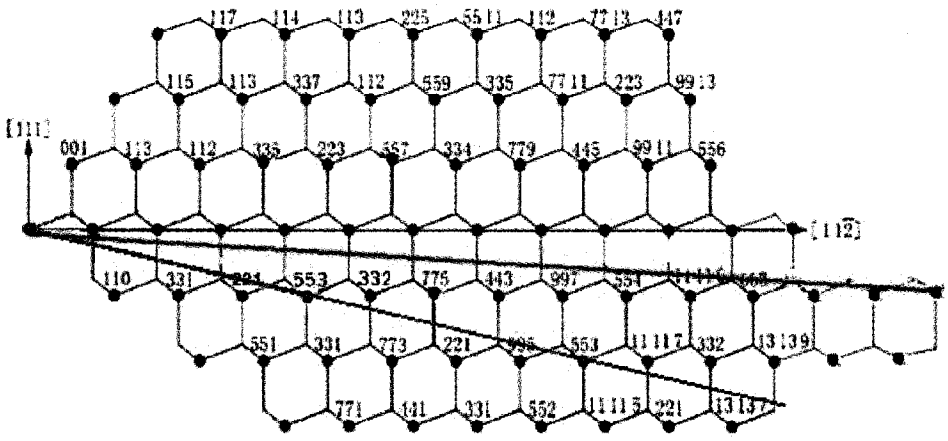

Figure 2-2-3 "Si road map" for vicinal silicon surfaces. The image represents a cut through the Si bulk crystal in the $(1\bar{1}0)$ plane. The dots indicate the position of Si atoms in the bulk and the black horizontal line in the middle of the crystal is the (111) plane. The red and blue lines represent the orientations of 3.8° and 12.3° samples respectively. Figure reproduced from Reference 30.

Several groups have investigated the gold induced surface restructuring of vicinal surfaces miscut towards $[11\bar{2}]$. Previously J.D.O'Mahony et al.[26] used STM to investigate samples oriented 4° towards $[11\bar{2}]$. Using their heating procedure, the clean surface consists of small (111) terraces separated by single height steps. At 0.1 ML, the surface exhibits larger (111) terraces (120 $\mathring{A}$ width) with 7x7 and 5x2 regions of equal width and regions of step bunching. The 5x2 regions are adjacent to the rising steps. As the coverage increases to 0.2 ML, the large (111) terraces with 7x7 and 5x2 regions grow (300-400 $\mathring{A}$). At 0.5 ML the entire (111) terraces exhibit a 5x2 reconstruction and regions of step bunching form a well defined (775) facet. The (775) facet is orientated 8.5° towards $[11\bar{2}]$ and characterized by 1-d chains orientated along the $[1\bar{1}0]$ direction spaced 21.3 $\mathring{A}$ apart. Beyond 0.5 ML, the (111) terraces transform to $a\sqrt{3}\,x\sqrt{3}\,R30°$ reconstruction.

L.Seehofer et al.[31] studied the structure of surfaces tilted 2°, 4°, 9°

towards $[11\bar{2}]$ at the 5x2 coverage of gold. In all cases, they found that the surfaces consisted of flat (111)5x2-Au terraces separated by regular (775) facets.

Shibata et al.[32] showed at 0.3 ML, 4° surfaces consist of large (111)7x7 terraces and well ordered (775) facets. They also found adatom-like structures on the step edge adjacent to the 7x7 terraces. These authors suggested that the (775) facet resembles a 5x2 unit cell modified to include an atomic step. As a result, the (775) facet represents a Au induced low energy facet on these surfaces.

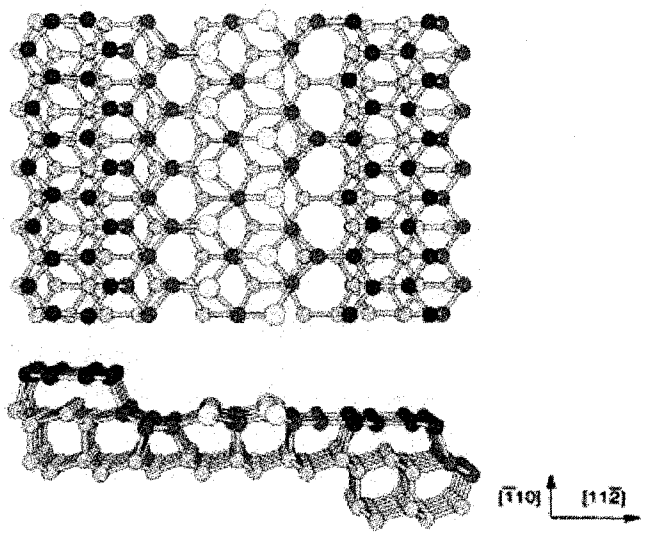

Figure 2-2-4 schematic view of (775), all the atoms have the same denotation as figure 2-2-2. Figure reproduced from Reference 30

Although the exact structure of the (775) surface is not known, one model proposed by J.N.Crain et al.[30] on the basis of photoemission measurements is shown in Figure 2-2-4. The Au adsorbed facet has a characteristic chain of spacing 21.3 $\mathring{A}$, and an inclination angle of 8.46° from the (111) plane.

R.Hild et al.[33] published a detailed LEED investigation of the structure of a 4.3° sample as a function of Au coverage and annealing temperature shown in Figure 2-2-5. According to their results the (775) facet appears on the surface

over a wide range of gold coverage (0.1- 0.46 ML). Beyond 0.5 ML the surface undergoes restructuring to (553) facets separated by flat (111) terraces. Below 0.75 ML, the (111) terraces are 5x2 reconstructed, while beyond 0.75 ML the (111) terraces are $\sqrt{3}\,x\,\sqrt{3}\,R30°$ reconstructed.

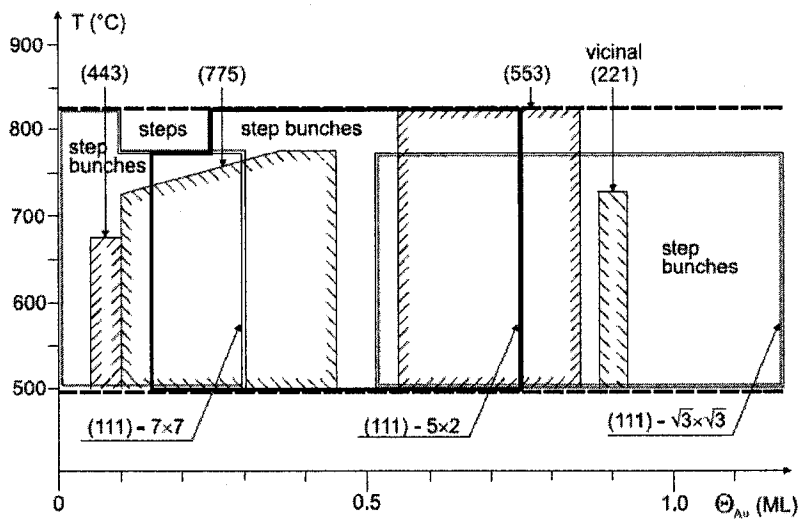

Fig 2-2-5 Structure diagram for a 4.3° vicinal Si (111) with the miscut towards the $[11\bar{2}]$ direction as a function of Au coverage and sample temperature. Figure reproduced from Reference 33.

On samples with a higher miscut M.Jalochowski et al.[34] observed ideal Si (755) facets at 0.2 ML of Au on samples orientated 9.44° towards $[11\bar{2}]$. Previously our lab has investigated the morphology of samples miscut 8° over a wide range of Au coverage (0 - 0.44 ML)[35]. It was found that well defined (775) facets are formed at the onset of gold deposition up to 0.32 ML. Below 0.18 ML, gold migrates exclusively to the (775) facets and non-(775) facets are gold free. In agreement with Hild et al.[33] beyond 0.32 ML, the surface forms steeper facets i.e. (332) and (553), with shorter chain spacing. Using UHV reflection electron microscopy Aoki et al.[36] observed (553) facets on samples miscut 12.3° towards $[11\bar{2}]$.

The (553) facet has been observed by several authors at higher gold coverage or on samples with a larger miscut. It is characterized by chains spaced $14.8\,\mathring{A}$ apart and oriented 12.3° towards $[11\bar{2}]$. While the exact nature of the (553) facet is unknown, Figure 2-2-6 illustrates a recent model based on first-principle density function calculations.

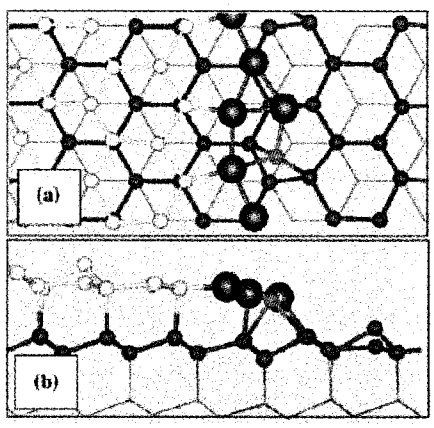

Figure 2-2-6 top (a) and lateral (b) view of the double row mode of the Si (553)-Au after 300 steps of unconstrained structural relaxation. Red ones are gold atoms and the rest are silicon atoms. Figure reproduced from Reference 37.

In this thesis we extend the work of these authors to study the gold induced morphology of samples miscut 3.8° and 12.3° towards $[11\bar{2}]$ as a function of gold coverage. These two wafers are chosen because 3.8° is below the 8.5° orientation of (775) facet while 12.3° is above it.

Chapter 3: Experimental Techniques

3.1 Instrumentation

3.1.1. UHV system

All of the work in this thesis was performed in an ultra-high-vacuum (UHV) chamber. The low pressure was necessary for the surface to maintain a stable composition. The UHV environment allows for low arrival rates of reactive species from the surrounding gas phase. The rate of arrival of atoms or molecules from a gas of density n and average velocity c_a, is [38]

$$r = \frac{1}{4} n c_a \tag{3.1}$$

Using the kinetic theory of gases, the rate of arrival can be rewritten to yield:

$$r = 3.51 \times 10^{22} P/(TM)^{\frac{1}{2}} \tag{3.2}$$

Where r is in molecules/(cm^2 s), P is in Torr, and M is the molecular mass in g/mole and T is in Kelvin. For example, in our UHV system, the pressure is kept below 2×10^{-10} Torr. At ambient temperature, and assuming a unity sticking coefficient, the time for a monolayer ($7.8 \times 10^{14} cm^{-2}$) of N_2 molecules (M=28) to accumulate is almost *5.6 hrs*, which is acceptable for our experiments. For comparison, in high vacuum (10^{-6} *Torr*), this period would be *2 s*.

Our experiment starts with the input of a sample into the UHV system through a load lock. The load lock is pumped to around 2×10^{-6} *Torr* before introducing the sample into the main chamber. The pressure in main chamber is kept below 2×10^{-10} *Torr*. The main chamber is a two level system with low energy electron diffraction (LEED) and Auger electron spectroscopy (AES) on the upper level, and a gold evaporator, load-lock, and scanning tunneling microscope (STM)

on the lower level.

To produce the UHV pressures required for our experiments, we use several pumps working together to achieve the ultimate pressure. The first stage of pumping is a mechanical pump. Gas enters the chamber of the pump and is compressed by a rotor and vane and then expelled to the atmosphere through a discharge valve. The oil-sealed unit pumps gases in the pressure range of *1* to $10^5 Pa$. We use an Edwards E2M2 pump[39], with a displacement of *10* to *200* m^3/h.

The next pumping stage we utilize is a turbomolecular pump[40]. This pump consists of a molecular turbine that compresses gases by momentum transfer from the high speed rotating blades (which in our case is *60,000 rev/min*). The relative difference in velocity between the slotted rotating blades and slotted stator blades is designed to transfer gas molecules from pump inlet to outlet. To evaluate the pump performance, we define two parameters, the first is the compression ratio, which is defined as the ratio of outlet pressure to inlet pressure, and the other parameter is the pumping speed.

Normally, the turbo pump works in the so-called molecular flow region. Molecular flow is defined in terms of two quantities; the Knudsen number K_n, and the Reynolds number *R*. The Knudsen number K_n is the ratio of the mean free path of the gas to the characteristic dimensions of the system. The Reynolds number *R* is defined as:

$$R=\frac{U\rho d}{\eta} \qquad (3.3)$$

where ρ is the mass density of the gas, η is the viscosity and U is the stream

velocity in a pipe of diameter d. Molecular flow occurs when $K_n > 1$, and $R < 1200$[39].

The ultimate pressure of the pump is determined by the compression ratio for light gases. One advantage of the turbo pump is that it does not backstream hydrocarbons from the lubricating fluid. We use a Varian Turbo-V60[41] model for initial pump down of the main chamber and to pump the load lock. The specifications of our turbo pump are listed in Table 3-1-1:

	Nitrogen:	Helium:	Hydrogen:
Pumping speed (l/s)	65	55	45
Compression ratio	$5x10^7$	$4x10^3$	$4x10^2$
Base pressure (Torr)	$8x10^{-10}$	$8x10^{-10}$	$8x10^{-10}$

Table 3-1-1 Specifications of Turbo-V60 Turbo molecular Pump[41]

The main pump in our system is an ion pump and is used to achieve UHV pressures. This pump is oil free, and it has no moving parts which is important for our vibration sensitive STM experiments. The potential difference between anode and cathode ($\sim 7kV$) in the pump along with an axial magnetic field forces the electrons from the cathode to travel in circular orbits. The circular path helps electrons travel long distances before reaching the anode and thus increases the probability of ionizing collisions with gas molecules. The ionized gas molecules can also trigger further ionization. The cations are accelerated towards the cathode and captured. In the process, they sputter away cathode material (Titanium). The freshly sputtered titanium is highly reactive and provides further pumping. The ion pump used in our system is a Varian, VacIon Plus 150 with a pumping speed of

150L/s, and a base pressure of 10^{-11} *Torr*[41].

To increase the pumping speed at our base pressure we also use two getter pumps; a titanium sublimation pump (TSP), and a non-evaporable getter pump (NEG). Titanium is used in the TSP because it has a high vapor pressure at much lower temperatures than most other metals and is highly reactive. The freshly evaporated Ti reacts with adsorbed gases. As the Ti film becomes saturated, a fresh titanium layer is sublimed periodically to ensure continual pumping. At UHV pressures, the Titanium layer lasts for at least *24 hours*.

The Capacitorr-D400 NEG pump[42], pumps by surface adsorption and diffusion into the bulk. During initial pump down of the chamber, the NEG pump needs to be activated by heating the getter material to 800° C for about an hour to diffuse the adsorbed gases into the bulk. This pump has an extremely high pumping speed for hydrogen (*1380 L/S*) which is the main residual gas in our chamber.

In spite of these pumps, there are always gas species outgassing from the walls. To achieve UHV pressures, the entire system must undergo a baking procedure. This procedure promotes diffusion out from the walls of the chamber. The entire chamber is heated to above 100° C and is held at this temperature for several days. Following the bake, it takes, one or two days for the chamber to cool down and reach an ultimate pressure of 10^{-10} *Torr*.

3.1.2 Low Energy Electron Diffraction

One of the primary experimental techniques used in the thesis is Low Energy Electron Diffraction (LEED), discovered by C.J. Davisson in 1927[43]. LEED is an

extremely powerful technique to investigate surface structure, since the mean-free-path for inelastic scattering of electrons is very short. At the energies used (*50-100eV*), electrons can travel elastically no more than two or three atomic layers.

The diffraction pattern measured in LEED represents an image of the surface atomic structure in reciprocal space. Defining the incident wave vector as $\vec{k}$ and the emerging wave vector as $\vec{k}'$, elastic scattering requires:

$$k^2 = k'^2, \tag{3.4}$$

in addition, in the surface plane, conservation of momentum requires:

$$\vec{k}'_{//} = \vec{k}_{//} + \vec{g}_{hk} \tag{3.5}$$

Where $\vec{g}_{hk}$ is a reciprocal lattice vector of the crystal lattice in the plane of the surface:

$$\vec{g}_{hk} = h\vec{a}^* + k\vec{b}^* \tag{3.6}$$

where $\vec{a}^* = 2\pi \frac{\vec{b} \times \vec{n}}{\vec{a} \bullet \vec{b} \times \vec{n}}$ and $\vec{b}^* = 2\pi \frac{\vec{n} \times \vec{a}}{\vec{a} \bullet \vec{b} \times \vec{n}}$

a and b are the real space lattice vectors, and $\vec{n}$ is a unit vector normal to surface.

For a surface, it is easy to demonstrate that the reciprocal lattice becomes a set of rods normal to the plane of the layer. The best method to illustrate this is the familiar Ewald sphere construction as shown in Figure 3-1-2-1. The Ewald sphere is a graphical representation of the conservation of energy and momentum. A reciprocal lattice rod passes through every point of surface reciprocal net normal to the surface. Diffraction occurs at all points where the Ewald sphere, which has a radius equal to the magnitude of the incident electron wave vector, intersects a

reciprocal rod. ι and ι_0 are the angles the incident and diffracted beams make with the surface normal respectively[44]. In our experiment ι_0 equals 0.

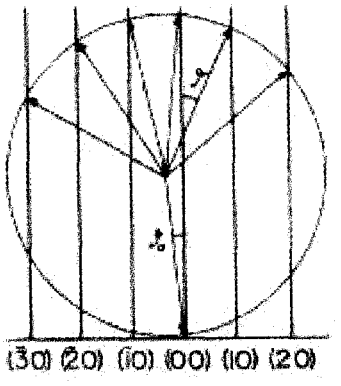

Figure 3-1-2-1 Reciprocal lattice for a single plane of atoms and Ewald construction for electron diffraction. Figure reproduced from Reference 44.

A schematic diagram of a typical LEED instrument is shown as in Figure 3-1-2-2. Electrons emitted by the gun are focused at normal incidence onto the surface of the sample. The electron gun is aligned along the central axis of the optics. The screen assembly consists of three or four concentric grids and a fluorescent glass screen with the centre of curvature at the sample position. The second and third grids are connected together. The grids are made from tungsten wire mesh and are gold coated to have a chemically inert surface with a uniform work function. The whole LEED optics is magnetically shielded by a Mu-metal tube. The first grid of the screen and the last electrode of the electron gun are held at the potential of the crystal, creating a field-free region for diffraction[41]. When low energy electrons are incident on a surface the majority of the electrons back-scattered from the crystal will lose energy in the scattering process (inelastic scattering). These electrons contain no diffraction information and have to be separated from the elastic contribution. This is achieved by applying a retarding

potential to the second and third grids that repels all electrons that have lost energy in the scattering process. The elastic electrons that pass through the retarding field are then accelerated to high energy and travel to the spherical fluorescent screen and create the diffraction pattern. The image is formed on a fused silica hemisphere coated with indium-tin oxide and high luminosity phosphor.

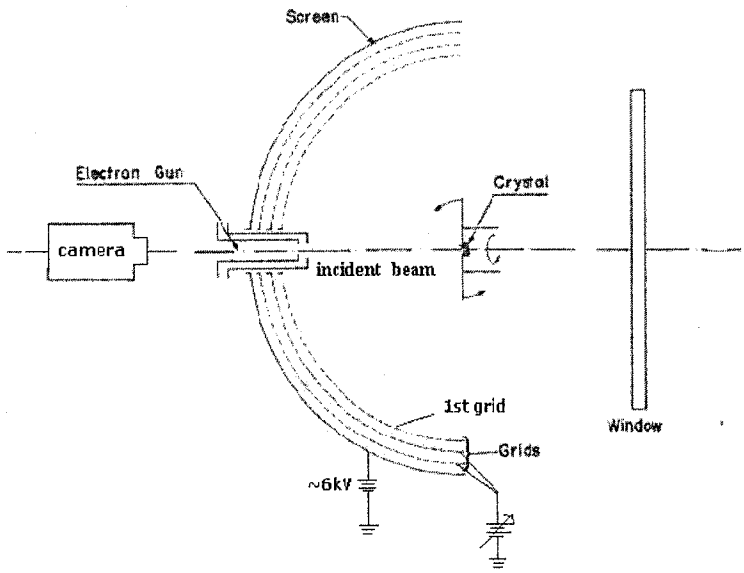

Figure 3-1-2-2 simplified LEED schematic. Figure reproduced from Reference 44.

The apparatus used in our UHV system was manufactured by OCI Vacuum Microengineering[44]. The LEED experiment is controlled by a LABVIEW program[45] and the image is recorded using a CCD camera.

In Figure 3-1-2-3, a LEED image of a clean Si (111)7x7 reconstructed surface is shown. In real space the reconstructed unit cell exhibits hexagonal symmetry. The cell is defined by real space vectors $|a_1| = 7a$ (outlined in part (a) of Figure 3-1-2-3) where a is the dimension of the bulk terminated lattice. In reciprocal

space this leads to a periodicity $|b_1| = \frac{2\pi}{7a}$ as illustrated in part (c) of Figure 3-1-2-3.

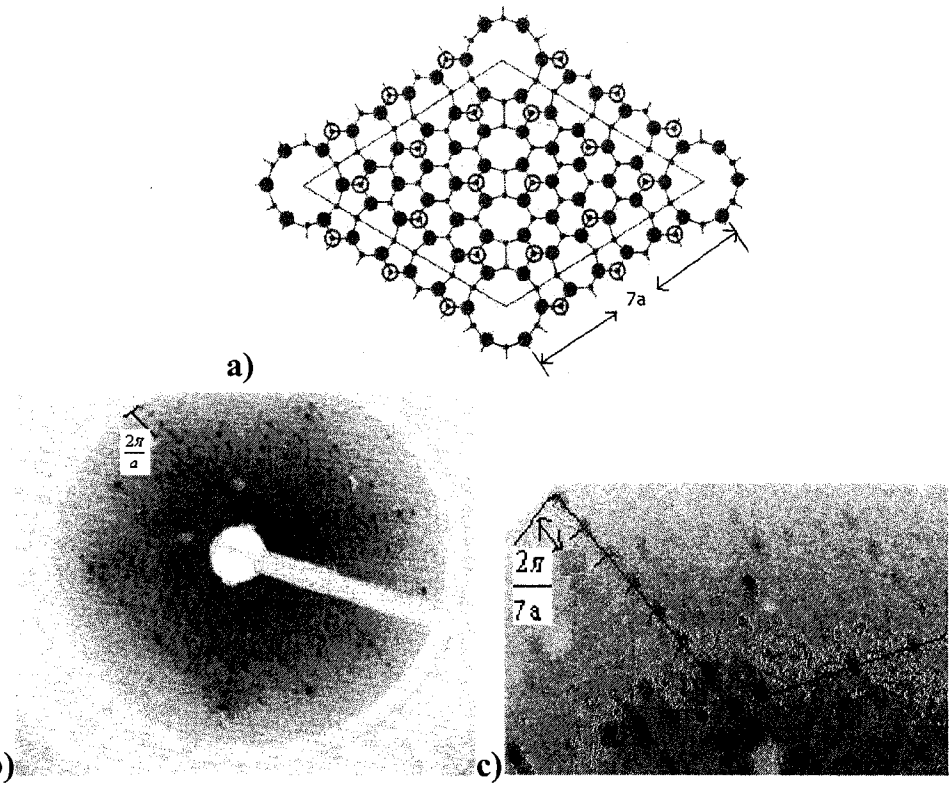

Figure 3-1-2-3 (a) A real space 7x7 unit cell model. Figure reproduced from reference 35 (b) A LEED diffraction pattern of the Si (111)-7x7 reconstruction taken from a clean 3.8° wafer at energy of 70 eV. The image highlights the dimensions of the bulk terminated cell. (c) Magnified portion of the image highlighting the $2\pi/7a$ periodicity associated with the reconstruction.

3.1.3 Auger Electron Spectroscopy

We used Auger Electron Spectroscopy (AES) named after its discoverer, Pierre Auger[46] to measure the surface composition of our samples. The Auger process is initiated by the creation of an ion with an inner electron shell vacancy. An electron from a higher lying energy level fills the inner shell vacancy along with the simultaneous emission of an Auger electron. This simultaneous two electron process results in a final state with two vacancies (Figure 3-1-3-1). In the

figure, the original ionization occurs in the K shell. To occupy the core hole, an electron in the L_{II} shell falls into the vacancy and the potential energy lost is transferred to a second electron in L_{III} leading to the emission of that electron. All the energies in Figure 3-1-3-1 are referenced to the Fermi energy E_f.

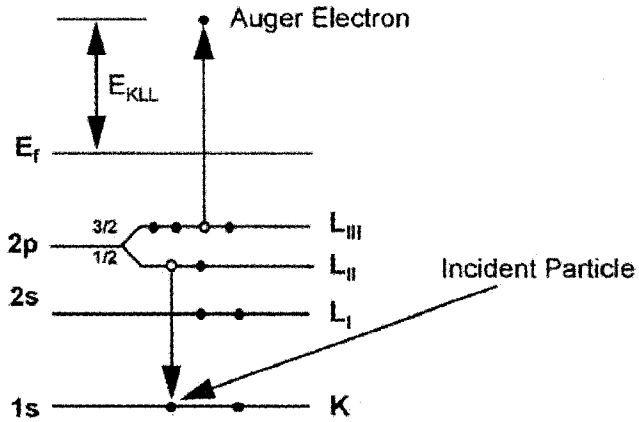

Figure 3-1-3-1 schematic diagram of an Auger electron emission process. Figure reproduced from Reference 46.

For a proper description of the kinetic energy of the Auger emitting electron, we can write,

$$KE=E_A-E_B-E_C-U \qquad (3.7)$$

Where E_A is the one-electron binding energy of the core electron level (K shell), E_B is the energy of the valence electron which drops into the K shell (L_{II} level), Ec is the energy of the initial energy level of the Auger electron (emitted from L_{III} level), and U is the hole-hole interaction energy.

The kinetic energies of emitted electrons for a number of specific Auger transitions are well known for many elements and used to identify the chemical composition of a surface. For example, in the left part of Figure 3-1-3-2 an undifferentiated Auger electron spectrum of the number of electrons as a function

of energy contains a contribution from the Carbon (KLL) Auger emission at an electron energy of around *275 eV*. On the right, the Auger spectrum is shown in the more conventional differential form with *dN/dE* as a function of energy. This mode has the virtue of suppressing the large secondary electron background and turns a simple peak in *N(E)* into a positive and negative excursion. It is common to define the peak energy in the differentiated spectrum as the energy of the largest negative excursion.

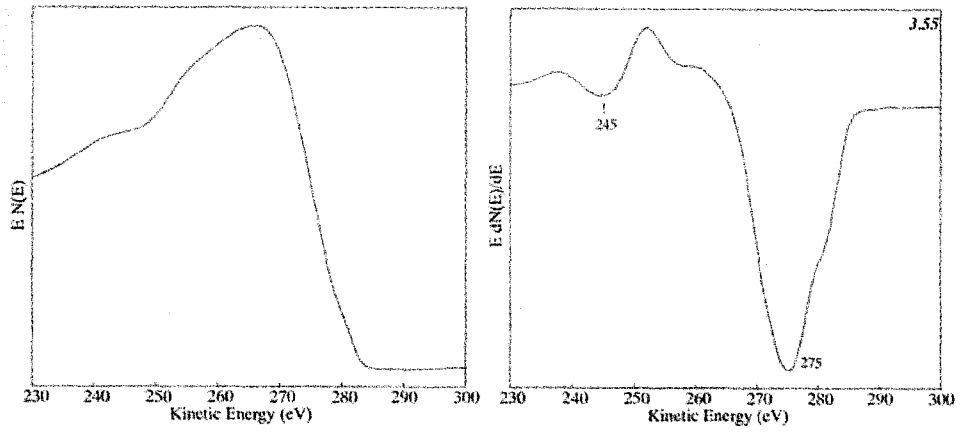

Figure 3-1-3-2 Two different modes to illustrate Auger electron spectra. Figure reproduced from Reference 46.

We obtain our AES data using a cylindrical mass analyzer (CMA) manufactured by Omicron GMBH[47]. The CMA was first introduced by Palmberg et al.[38] in 1969.

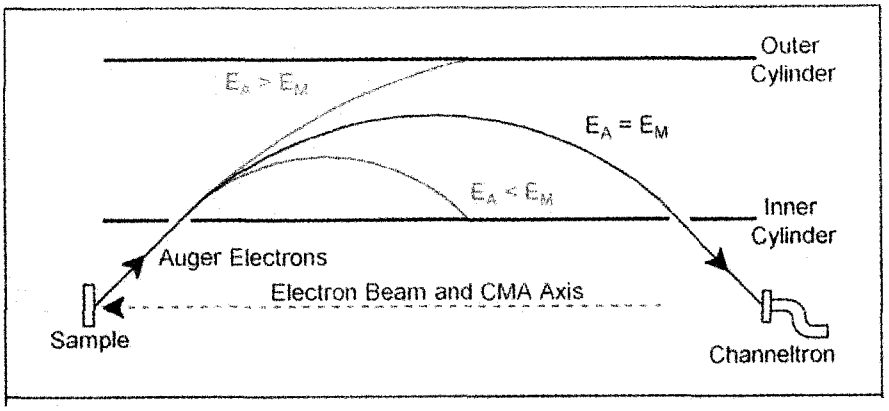

Figure 3-1-3-3 Schematic representation of a cross section of the upper half of the Cylindrical Mirror Analyzer. This diagram illustrates the energy selectivity of the analyzer. Figure reproduced from Reference 46.

A schematic cross section of the upper half of a typical CMA is shown in Figure 3-1-3-3. The figure illustrates the energy selectivity of the analyzer. Energy selectivity is provided by a radial electric field between the inner and outer cylinders. Auger electrons with energy equal to the E_M defined by the electric field are able to travel to the channeltron and be detected.

Figure 3-1-3-4 is an example of an Auger spectrum taken in our lab of the clean Si(111)7x7 surface. As can be seen from the spectrum, the largest peak in the low energy range always shows up at energy of *96 eV*, corresponding to the Si_{KVV} peak. We use AES to evaluate the cleanness of the surface as the technique can detect surface contaminants down to 7.8×10^{12} *atoms/cm*^{2}, or *1* percent of a monolayer[46]. The most common contaminant for our surface is carbon which appears around *270 eV*[46]. If the sample is not heated properly, or has not been degassed at an appropriately elevated temperature for a sufficient period of time, the AES spectra will exhibit a small carbon peak.

We also use AES is to determine the gold coverage by measuring the ratio

between the gold (*48 eV*) and silicon (*96 eV*) peaks. At low coverage, the ratio of these peaks decreases linearly with Au coverage.

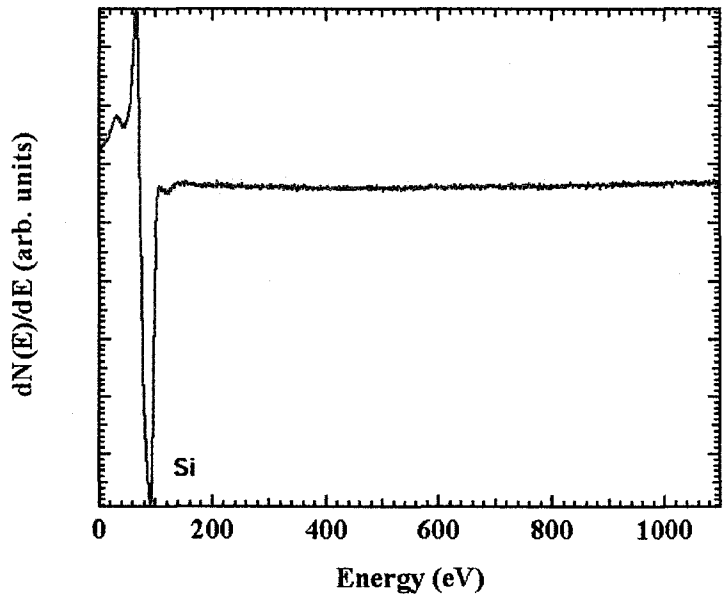

Figure 3-1-3-4 Auger spectra taken on a clean 3.8° sample surface at energy of 72 eV.

3.1.4 Scanning Tunneling Microscopy

The primary experimental technique used in this thesis is Scanning Tunneling Microscopy (STM) as invented by Binnig, Rohrer and Gerber[48] in 1981, and which led to the awarding of a Nobel Prize in Physics to Binnig and Rohrer in 1986.

3.1.4.1 Quantum Theory of Tunneling

STM relies on the quantum mechanical phenomena of vacuum tunneling. Tunneling is a process by which particles can traverse potential barriers at energies which are classically forbidden. In vacuum tunneling, the potential in the vacuum region acts as a barrier to electron travel between two electrodes. The two electrodes can be metals or semiconductors. In our case we have a Si surface and a metallic STM tip.

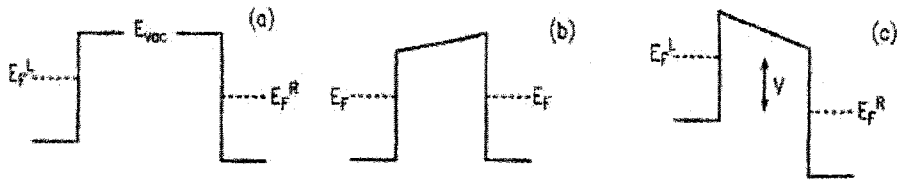

Figure 3-1-4-1 schematic of potential barrier for vacuum tunneling. (a) When separated the Fermi level of two electrodes differs by an amount equal to the work function difference. (b) When the electrodes are connected electrically the Fermi levels align (c) If a voltage is applied between the electrodes a net tunnel current can flow. Figure reproduced from Reference 15.

For tunneling to occur between two electrodes a voltage difference V is applied across the gap and filled states within energy eV of the Fermi level can tunnel into the empty states on the other side.

From quantum mechanics the transmission probability, and thus the tunneling current I, decays exponentially with barrier width d as

$$I \propto e^{-2kd} \tag{3.8}$$

where $k^2=2m(\phi-E)/\hbar^2$, ϕ is the barrier height, and E is the kinetic energy of the electrons. Since most work functions are around *4-5 eV*, this leads to a decay constant k of the order of $1\ \text{Å}^{-1}$. For voltages of the order of a volt, a typical barrier width of $9\,\text{Å}$ produces a tunnel current of several nanoamps. In addition, the tunneling current drops nearly an order of magnitude for every $1\,\text{Å}$ increase of the separation. This exquisite sensitivity to separation is ultimately responsible for the success of STM. The STM uses current feedback to maintain a constant tip-surface distance as it is scanned above a surface to produce a topographic image. More specifically the STM maps contours of constant surface charge density.

It is not easy to write down an exact expression for the tunneling current in

realistic 3-d tunneling. Amongst various approximations, the Tersoff and Hamann approach[49] is the most widely used. They treat the surface "exactly", and the tip is modeled locally as a spherical potential. Based on first-order perturbation theory, Bardeen[50]developed an expression for the electron current between two electrodes.

$$I = \frac{2\pi e}{\hbar} \sum_{\mu,\nu} f(E_\mu)[1 - f(E_\nu + eV)] \left|M_{\mu\nu}\right|^2 \delta(E_\mu - E_\nu) \tag{3.9}$$

Where $f(E)$ and $f(E_\upsilon + eV)$, are the Fermi functions in the tip and sample respectively, V is the applied voltage, and $M_{\mu\nu}$ is the tunneling matrix element between states ψ_μ and energies E_μ in the tip, and ψ_ν and E_ν in the surface. At room temperature, in the limit of small voltage, and by replacing the tip by an ideal point source of current, Tersoff and Hamann showed that Equation (3.9) reduces to:

$$I \propto \sum_{\nu} \left|\psi_\nu(\vec{r}_0)\right|^2 \delta(E_\nu - E_F) \tag{3.10}$$

The quantity on the right of the above Equation is defined as the surface local density of states (LDOS) of the surface at the position of the tip, $(\vec{r}_0)$. Thus, the STM image is a contour map of constant surface LDOS.

3.1.4.2 Tip Preparation and STM Instrumentation

A schematic diagram of an STM is shown in Figure 3-1-4-2. Our STM is an Omicron Micro SPM[47], and we control the STM with SPM 32 software from RHK Technology Inc[51].

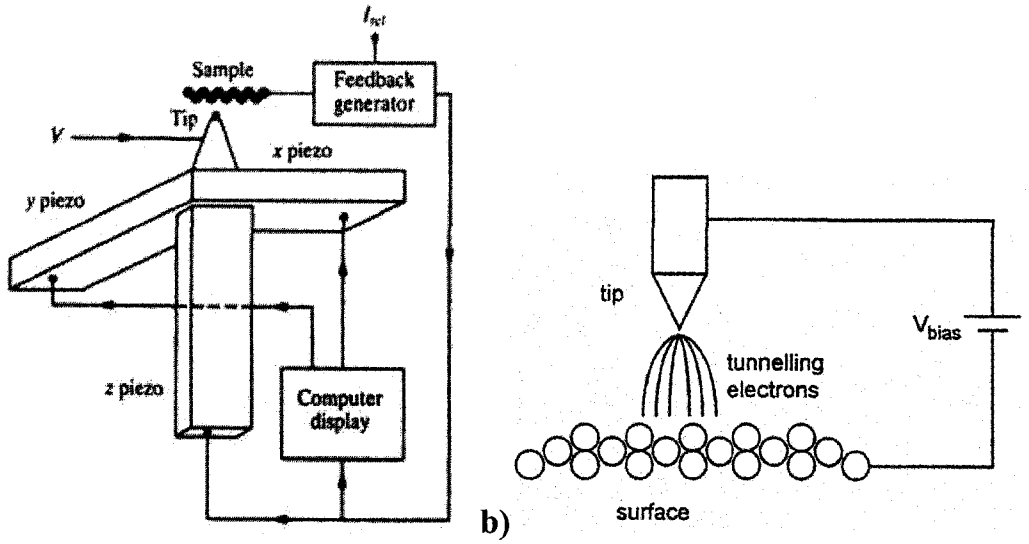

Figure 3-1-4-2 a) Schematic diagram of an STM. Figure reproduced from Reference 38. b) Illustration of STM operation. Figure reproduced from Reference 47.

Prior to tunneling; the tip and associated scanner must be brought into tunneling distance in a very precise manner. Our STM uses an inertial coarse approach system where a voltage is applied to a piezoelectric stack. By applying voltage to the elements in the stack it extends towards the sample. The scanner and tip are mounted on the stack and move with it, but when the stack is quickly contracted the inertia of the scanner keeps it and the tip in place. The result is a net displacement (around 400nm) of the scan and tip with respect to the sample. To prevent the tip from crashing into the sample, the feedback contracts the scanner and moves the tip away from the sample during the inertial step. The tip relaxes back after the step and if no tunneling current is detected, the former process repeats.

Once in tunneling distance, the tip is raster-scanned across the surface without crashing into the sample. The distance between sample and tip is maintained within $0.05\,\mathring{A}$. Both of these functions are fulfilled by a single

piezoelectric scanner tube. The tip sits on the top of a hollow tube. To allow for X, Y and Z motion the outer electrode of the tube is etched into four quadrants and the inner electrode is grounded. Applying a voltage difference between opposite quadrants moves the tip in a parallel direction (X or Y). Applying a voltage uniformly to all four quadrants moves the tip in the Z direction.

Obviously the success of any STM experiment depends on the preparation of a sharp tip. In our experiment, we make the STM tips out of two materials, tungsten and a PtRh alloy. To prepare tungsten tips, we use an electrochemical etching technique[47],where we cut a piece of tungsten wire and hang it through a drop of *1* molar NaOH solution. An AC voltage is applied between the tungsten wire and an annular ring that holds the NaOH drop. The field completely etches through the tungsten and the bottom portion of the tip below the ring falls. After rinsing the fallen wire in distilled water, the tip is ready to be introduced into the UHV chamber. Normally, there is still an oxide layer on the tip, and the oxide is removed by field emission in vacuum. We also utilized PtRh tips which were simply prepared by cutting a piece of wire.

As mentioned, W tips often require an additional step prior to use. Field emission is produced by applying a high accelerating electric field (several hundred electron volts) between the tip and the metal surface. Field emitted electrons bombard the tip and can induce electron stimulated desorption of the oxide or other contaminants.

Vibration isolation is also critical if atomic resolution is to be achieved. Our STM sits on a Viton stack inside the UHV chamber to dampen any vibrations. In

addition, the entire UHV system is pneumatically levitated while imaging.

3.2 Sample Preparation

3.2.1 Clean surface preparation

To ensure the cleanness of the sample surface, handling outside the UHV system needs to be done with gloves. In addition, to avoid Ni contamination no steel tools can be used.

The wafers we use are n-type samples cut either 3.8° or 12.3° from the Si(111) plane towards $[11\bar{2}]$ and placed in a specially designed sample holder. The sample holder consists of two electrically isolated metal halves each with a Ta wire loop spotted welded onto them. The sample is mounted between the two loops to allow current to flow between the two halves through the sample. To ensure straight steps, the samples are mounted as stress free as possible and aligned so that the current travels parallel to the $[1\bar{1}0]$ step direction. Applying a current parallel to the step edge avoids electromigration effects which complicate the step morphology[52]. Once inside the main chamber, the sample is introduced to the vacuum chamber via a load lock, and the load lock is pumped to below 2×10^{-6} *Torr*.

The samples are prepared using a heating sequence outlined by L.Lin et al.[21]. The first stage of preparation is degassing of both the sample and holder at 650° C for one hour. This is below the temperature at which the Si surface oxide is removed. Following degassing, we wait for one hour to allow the pressure in the chamber to recover before calibrating the temperature on the sample. To calibrate the temperature we use an Ircon Ultimax Plus UX20P[53] infrared pyrometer with

the emissivity set to *0.4*. To prepare the sample, we use the following sequence. The sample is flashed to 1260° C for *10 s* to diffuse residual surface carbon into the bulk, and then cooled to 1060° C in *1 min*. At 1060° C single atomic steps are stable[33]. The critical part in the procedure is a slow cool down from 1060° C to 850° C at a rate of 0.5° C/s or slower. This is necessary to allow for the development of regular arrays of bunched steps. According to R.J.Phaneuf et al.[54,55], 850° C is the transition temperature for the silicon surface to transform from (7x7) to (1x1). How the sample is cooled through this critical temperature will affect the facet width and step density. A *30 min* post-anneal at 650° C is also applied to allow the bunched steps to reach a self-limiting size.

Following heating, AES is used to verify surface cleanliness and LEED is used to ensure long range order. A comparison of two Auger spectra before and after cleaning is shown in the Figure 3-2-1. Before cleaning, the spectra exhibits oxidized silicon peaks at around *80 eV*, a carbon peak at *270 eV*, and an oxygen peak at *510 eV*. Following the cleaning, AES reveals a strong Si peak at *96 eV*.

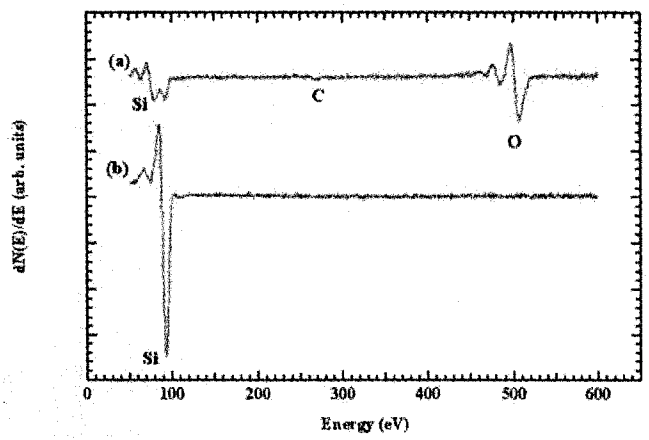

Figure 3-2-1 Auger spectra of (a) Si with carbon and an oxide layer. (b) Clean surface after removing the oxide layer.

In addition to AES, we also use LEED to ensure a suitable starting surface. A sharp LEED pattern is further evidence of a clean well prepared surface.

3.2.2. Au evaporator

We deposit Au using a Au filled tungsten basket. To calibrate the Au flux, we use the coverage dependent evolution of the LEED pattern on a flat Si(111) sample in combination with AES. From previous work we know that the 5×2 and $\sqrt{3}\times\sqrt{3}$ reconstructions occur at 0.44 and 0.9 ML respectively[56,57]. In addition to a LEED measurement, an AES spectrum is taken at each coverage. We obtain a graph of the Auger ratio of the Si/Au peaks as a function of gold coverage. Since the flux is constant, the coverage on the surface is proportional to time. To convert the time axis to coverage, we correlate AES with the optimized LEED images at 0.44 and 0.9ML. The result allows us to determine the coverage based on the Auger ratio at any intermediate exposure.

We deposit Au onto the silicon surface using the following procedure. First, the evaporator is brought up to evaporation temperature and the flux is stabilized by waiting for *60 s*. The sample temperature is stabilized at 650° C. The sample is then exposed to the Au flux for the required time. After deposition, the sample is annealed at 850° C for two minutes.

To reduce thermal drift, we wait for approximately two hours prior to STM measurements. Results indicate that at a base pressure of 10^{-10} Torr, samples can be imaged for several days with no apparent change in surface quality. Experiments also indicate that we can only investigate one Au coverage per sample. Attempts to deposit more Au onto a surface following STM experiments

result in a poor quality surface.

Chapter 4: Results

4.1 Morphology of 3.8° samples as function of Au coverage

We have investigated the Au dependent morphology of a vicinal Si wafer with a miscut angle of 3.8° toward [11$\bar{2}$]. The deposition of a submonolayer of Au onto this surface alters the surface morphology and ultimately produces 1-d chain-like reconstructions.

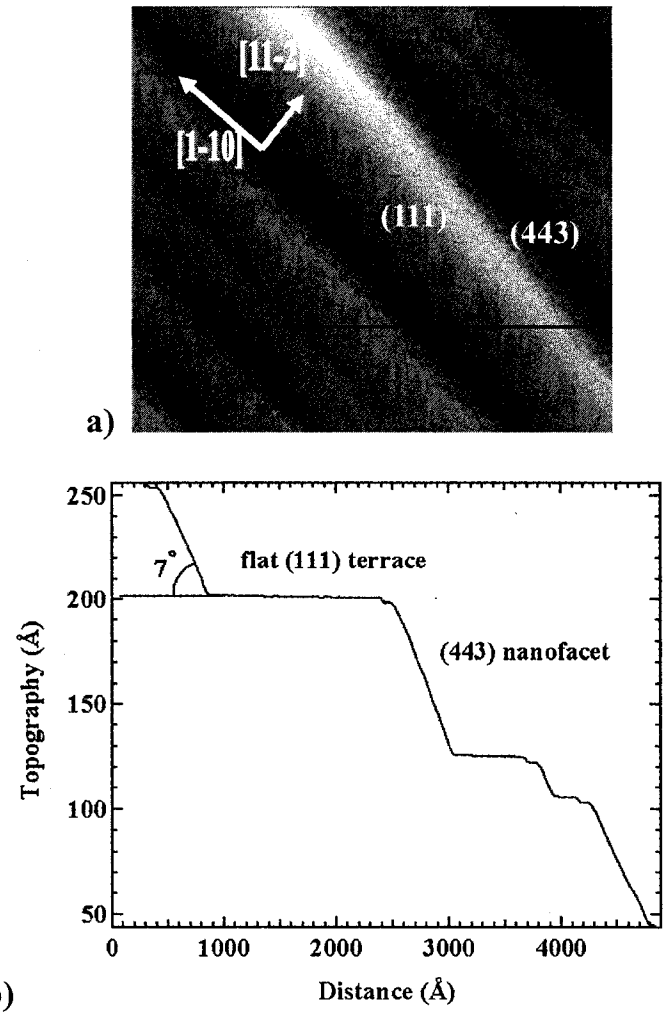

Figure 4-1-1 (a) An STM image (5000 Å ×5000 Å) of a clean 3.8° off-axis sample taken at a bias of +2.32 V with a PtRh tip. (b) A line scan corresponding to the black line in (a). The nanofacets are tilted 7° with respect to the (111) plane.

According to Equations (2.1) and (2.2) (assuming m=1) the 3.8° orientation

nominally corresponds to a (15 15 13) facet. This facet is not stable on the clean surface and instead, the surface consists of well defined (111) terraces with a 7x7 reconstruction and regions of step bunching, with atomic steps running along the $[1\bar{1}0]$ direction.

Figures 4-1-1(a) is an STM image of a clean 3.8° sample where the large regions correspond to flat (111) terraces. A cross sectional cut through the image, corresponding to the black line in part (a), is obtained by first flattening the terraces using the "plane subtract" macro in the SPM32 software[50]. In agreement with Lin et al.[21], the steps bunch to form facets tilted at an angle of 7° with respect to the (111) plane and once again using equation (2.1) and (2.2) with m=1, corresponds to a (443) facet. Although the sample in figure 4-1-1 was cooled slowly from 1060 to 850° C, we found the resultant morphology to be independent of the cooling rate.

Even at Au coverage as low as 0.04±0.03 ML, the surface structure undergoes dramatic changes. The large (111) terraces on the clean surface are no longer present, but as seen in Figure 4-1-2, the surface is now composed of small (111) terraces with steps running along the $[1\bar{1}0]$ direction. It is clear that Au deposition has dramatic effects on step-step interactions and the steps are far less bunched than on the clean surface.

The introduction of a small number of Au atoms onto the surface also induces the formation of chain structures at step edges (Figure 4-1-3). The STM image reveals two (111) terraces and a chain-like structure is apparent at the step edge. The LEED also develops weak streaks running along $[11\bar{2}]$ consistent with initial

chain formation (Figure 4-1-2 (b)). As with the clean surface, the Au induced restructuring at this coverage is insensitive to the rate of cooling.

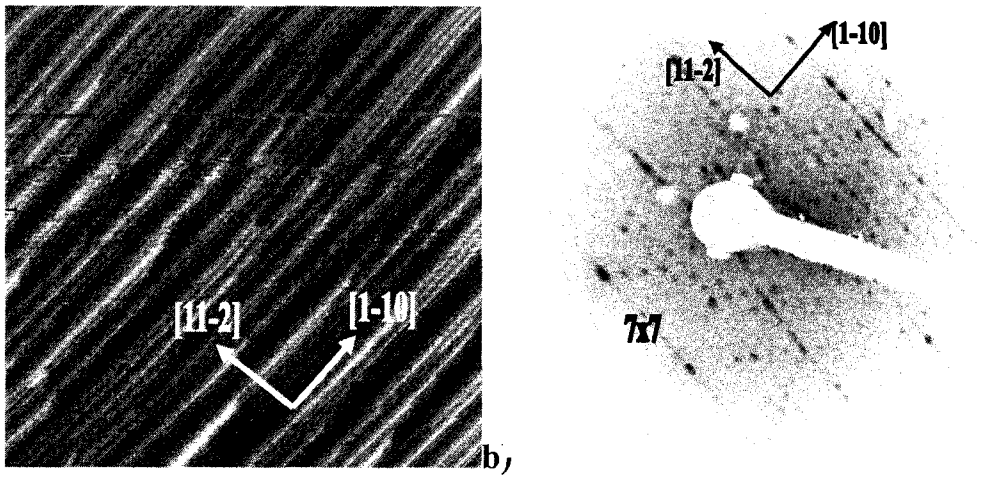

Figure 4-1-2 (a) An STM image (4980 Å ×4610 Å) of a 3.8° sample following 0.04±0.03 ML of Au. The image was taken at a bias of +2.4 V, with a PtRh tip. (b) Corresponding LEED image was obtained at 72 eV.

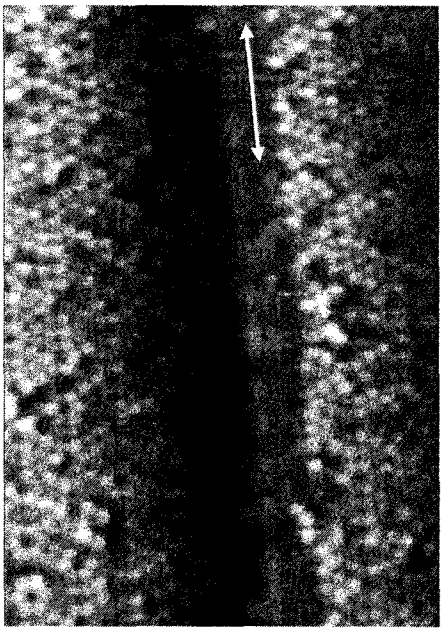

Figure 4-1-3 An STM image (220 Å ×290 Å) of a 3.8° sample following 0.04±0.03 ML of Au. The image was taken at a bias of -2.49 V with a tungsten tip. The arrow highlights the location of a 1-d structure at the step edge.

With higher coverage (0.12-0.20 ML), the steps which were initially

separated coalesce once again and the (111) terraces become larger than at 0.04 ML. At 0.18 ML for example, the step bunches form facets with an overall angle of 7.8° (Figure 4-1-4). At this stage the (111) terraces are still 7x7 reconstructed and gold free. Since the 7x7 reconstruction still dominates on the flat terraces, this indicates that all the adsorbed gold is incorporated at the steps. The LEED in part (c) shows further evidence of streaking consistent with facet formation.

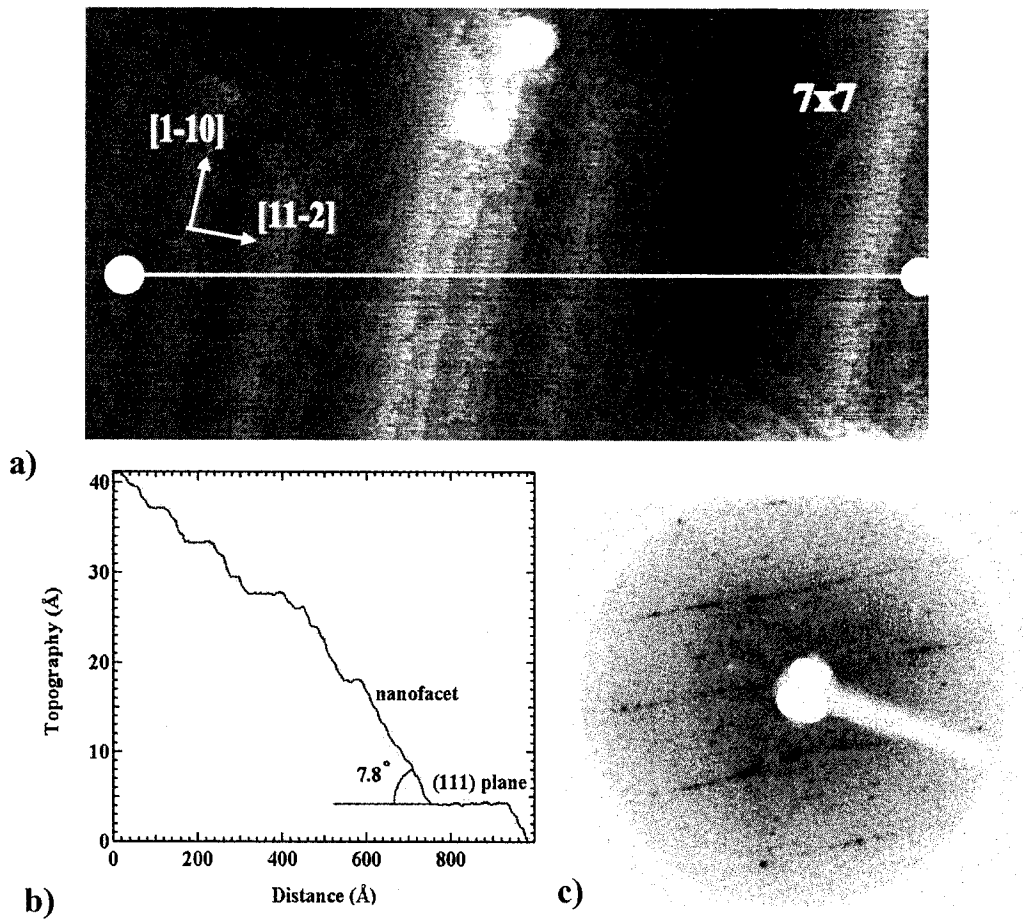

Figure 4-1-4 (a) An STM image (430 Å ×1000 Å) of a 3.8° sample following 0.18±0.03 ML of Au. The image was taken at a bias of +2.46 V, with a tungsten tip. (b) Corresponding line scan. (c) LEED image of a 3.8° sample following 0.12±0.03 ML of Au, taken at energy of 73 eV.

With increased Au, within the areas of step bunching, the step spacing

becomes more regular (Figure 4-1-5). In addition, at 0.20 ML STM measurements also reveal that the large flat (111) terraces now exhibit 5x2-Au reconstruction. Despite the 5x2 reconstruction on the large terraces STM indicates that in the regions of step bunching the smaller terraces still exhibit a 7x7 reconstruction. Contrary to our previous results on 8° samples[35], the presence of the 5x2 reconstruction on the large terraces indicates that gold is adsorbed on the flat terraces prior to the formation of well formed facets.

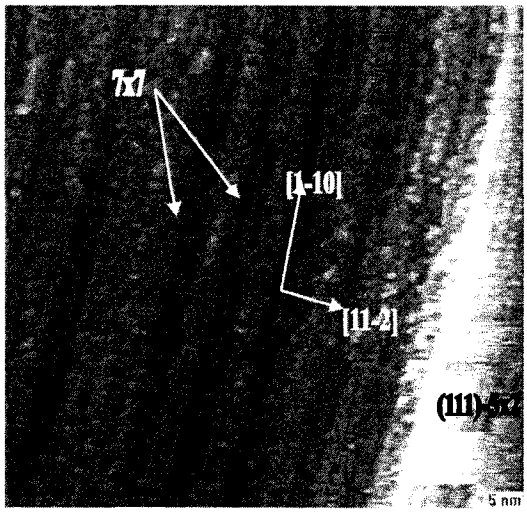

Figure 4-1-5 (a) An STM image (850 Å ×850 Å) of 3.8° sample following 0.20±0.03 ML of Au. The image was obtained at a sample bias of -2.52 V, and a current of 72.9 pA, with a tungsten tip.

At still higher coverage, the terrace spacing within the regions of step bunching becomes even more regular. In the STM image in Figure 4-1-6, the steps exhibit a striking 60.5 Å periodicity. The periodic terraces are comprised of small (111)7x7 terraces.

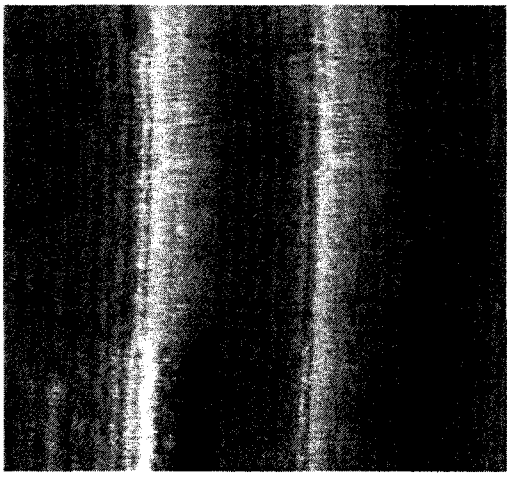

Figure 4-1-6 An STM image (2830 Å ×2830 Å) of a 3.8° sample following 0.28±0.03 ML of Au. The image was taken at a bias of +2.06 V, and a current of 427 pA, with a tungsten tip. (b) Corresponding LEED image at Au coverage of 0.28 ML.

Figure 4-1-7 was obtained at a gold coverage of 0.25 ML. Once again, the image exhibits large 5x2 terraces separated by regions of step bunching. On closer inspection the steps exhibit chains with several chain spacings (Figure 4-1-8).

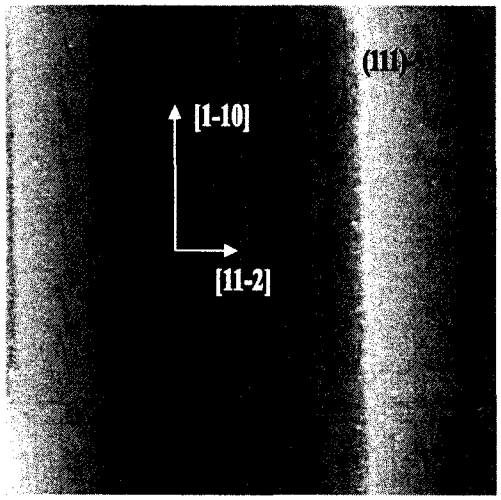

Figure 4-1-7 An STM image (1000 Å ×1000 Å) of a 3.8° sample following 0.25±0.03 ML of Au. The image was obtained at a bias of +2.74 V, and a current of 0.5 nA, with a tungsten tip.

In Figure 4-1-8 there are at least three different chain structures present. The chains are characterized by 1-d structures running along $[1\bar{1}0]$, with a well defined periodicity along $[11\bar{2}]$. Some chains are spaced 21.3 Å and define a (775) facet,

however other chain spacings are also evident. To the left of the (775) facet is a regular chain structure with a spacing of 32.9 Å, and to the right is a region with a chain spacing of 36.7 Å. According to the Equations (2.1), (2.2) and (2.3) these spacings correspond to (11 11 9) and (665) facets respectively.

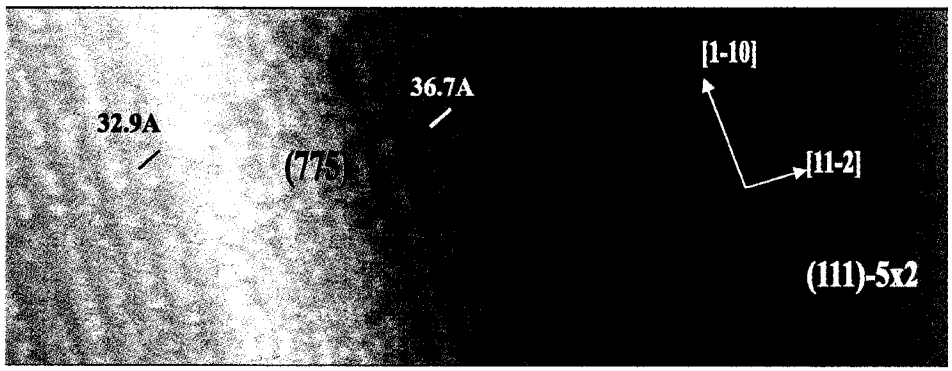

Figure 4-1-8 An STM image (340 Å × 1000 Å) of a 3.8° sample following 0.24±0.03 ML of Au. The image was obtained at a bias of -2.37 V, and a current of 1.18 nA, with a tungsten tip.

With increasing coverage, the step bunches continue to evolve into well-defined facets. A single chain structure starts to emerge. The chain spacing is close to 21 Å. In addition, the LEED exhibits well-defined spots indicating regular chain spacing along $[11\bar{2}]$ (Figure 4-1-9).

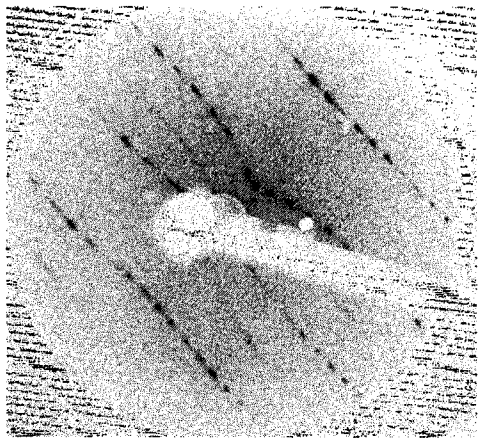

Figure 4-1-9 A LEED image obtained at 72 eV of a 3.8° sample following 0.35±0.03 ML of Au.

At 0.43 ML, the surface develops a well defined hill-valley structure as shown in Figure 4-1-10. The LEED image Figure 4-1-10(b), exhibits a

superposition of spots associated with the 5x2 reconstruction on the (111) terraces, and extra spots associated with the (775) facet. Furthermore, from the corresponding line scan (Figure 4-1-10(b)) the angle between the (111) terraces and facets is 8°. The transformation to a surface with (111)5x2 terraces and (775) facets is also evident in Figure 4-1-11. This coverage is similar to that necessary to optimize the (5x2) reconstruction for on-axis wafers[57,23].

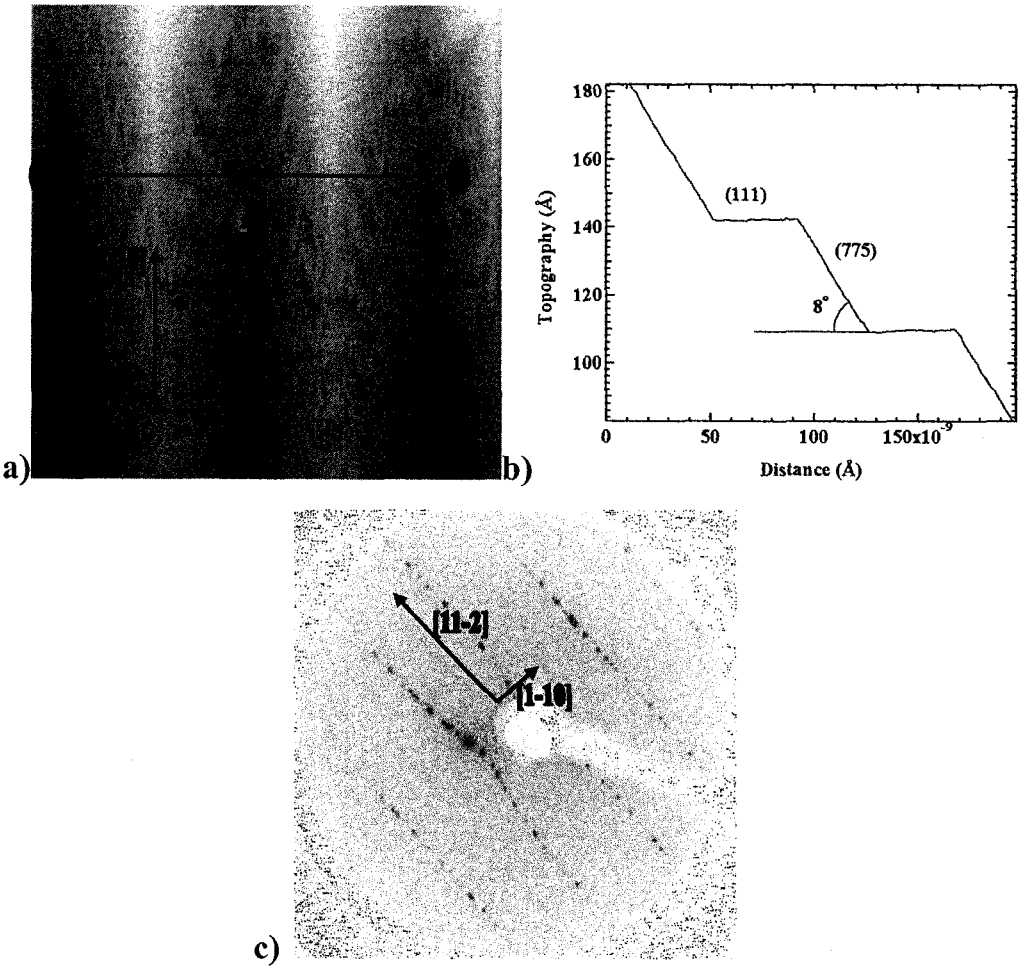

Figure 4-1-10 (a) An STM image (2000 Å ×2000 Å) of a 3.8° sample following 0.43±0.03 ML of Au. The image was taken at a bias of +2.09 V, and a current of 194 pA, with a tungsten tip. (b) Corresponding line scan. (c) LEED image taken at energy of 72 eV.

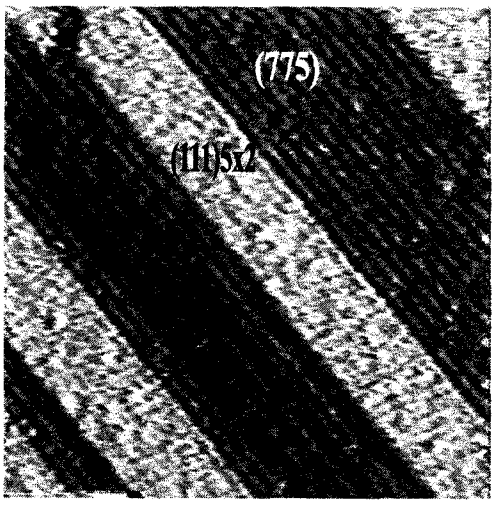

Figure 4-1-11 An STM image (700 Å × 700 Å) of a 3.8° sample following 0.44±0.03 ML of Au. The image was taken at a bias of -2.45 V, and a current of 199 pA, with a tungsten tip.

Beyond 0.44 ML the surface maintains a well-defined "hill-valley" structure (Figure 4-1-12), however the second facet now has an orientation of 12° with respect to the (111)5x2 terraces . This angle corresponds to the Au-induced (553) facet. This assignment is further verified in Figure 4-1-13, where the 12° facet consists of chains spaced 14.1 Å apart as expected. It has been shown previously that the local Au coverage on the (775) facet is 0.24 ML[35]. On the 8° sample, with increasing gold coverage the surface needs to form steeper facets with shorter chain spacing to accommodate more gold, i.e. 14.1 Å for the (553) facet versus 21 Å for the (775).

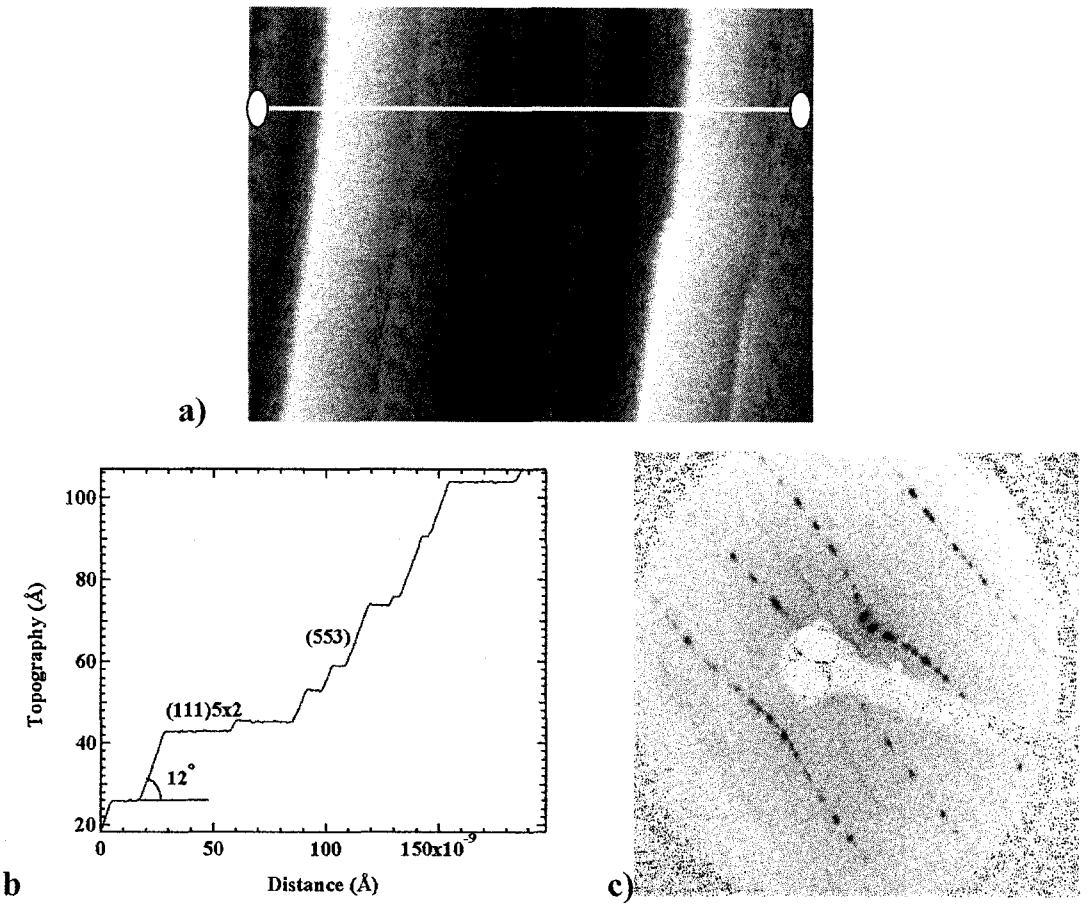

Figure 4-1-12 (a) An STM image (1990 Å × 1260 Å) of a 3.8° sample following 0.46±0.03 ML of Au. The image was taken at a bias of +2.48 V, and a tunnel current of 61.8 pA, with a tungsten tip. (b) Corresponding line scan. (c) LEED image taken on the same sample at energy of 72 eV.

Figure 4-1-13 An STM image (70 Å × 460 Å) of a 3.8° sample following 0.46±0.03 ML of Au. The image was taken at a bias of +2.05 V, and a current of 166 pA, with a tungsten tip.

4.2 Morphology of 12.3° samples

We have also investigated the Au-induced morphology of wafers miscut 12.3° towards $[11\bar{2}]$. This angle exceeds the 8.5° miscut of the (775) facet. On the 12.3° sample, (111) terraces are not stable, even on the clean surface. In all cases studied, the surface exhibits 1-d structures running along $[1\bar{1}0]$. The periodicity and degree of order of these structures depend on the gold coverage.

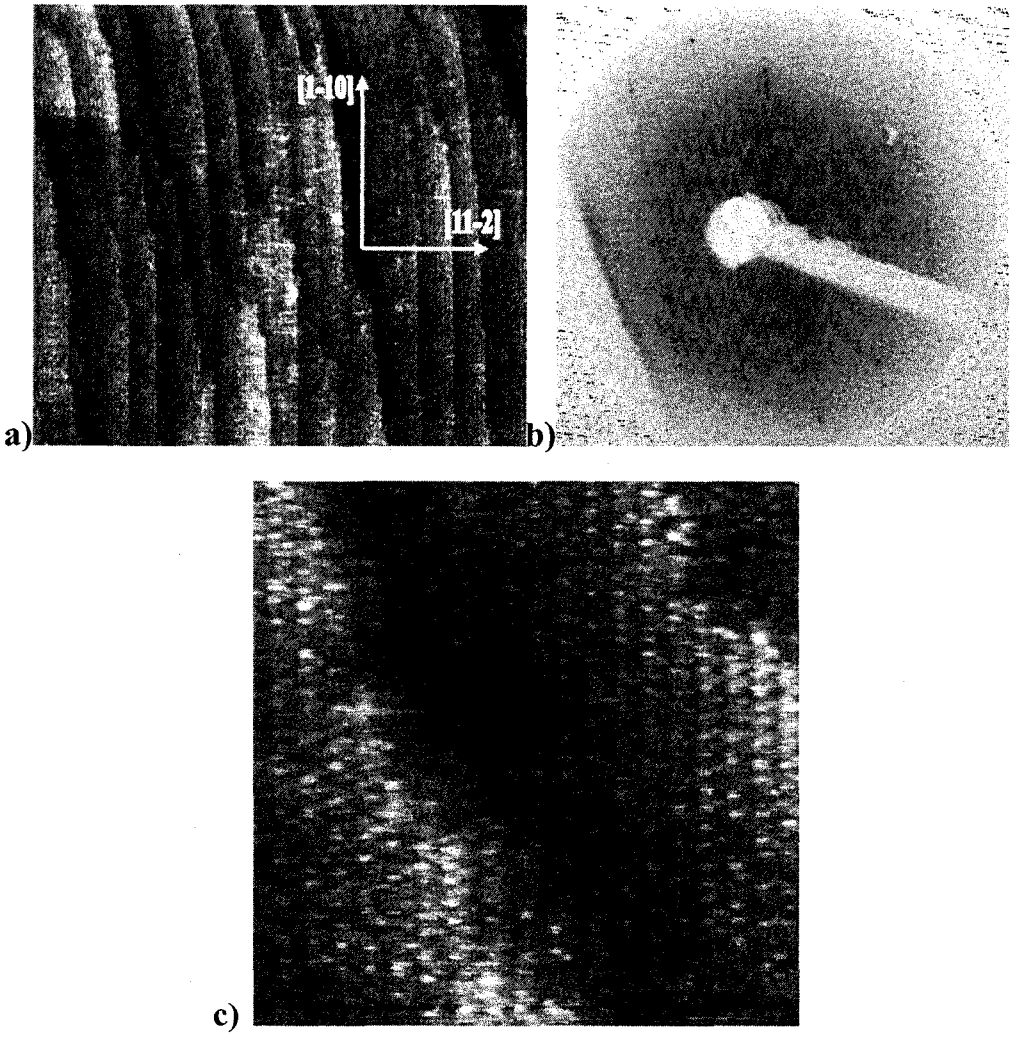

Figure 4-2-1 (a) An STM image (3000 Å × 3000 Å) of a clean 12.3° wafer, taken at a bias of +2.4 V, and a current of 323 pA, with a PtRh tip. (b) Corresponding LEED image at 96 eV. (c) An STM image (510 Å × 510 Å) of a clean wafer taken at a bias of +2.4 V, and a current of 260 pA, with a PtRh tip.

Figure 4-2-1 shows STM and LEED images of the clean surface. The STM image reveals large terraces consisting of 1-d structures separated by atomic steps. The periodicity of the chains is $26\,\mathring{A}$. If we measure the step height between each terrace, we find that it is quantized in units of about $1.4\,\mathring{A}$. On closer inspection each chain exhibits periodic spots along the $[1\bar{1}0]$ direction. The periodicity along $[1\bar{1}0]$ is $22\,\mathring{A}$.

From the LEED pattern in part (b), we observe uniformly spaced spots along the $[11\bar{2}]$ direction. Based on this periodicity, we calculate a chain spacing of $27\,\mathring{A}$ which is consistent with the STM.

As with other vicinal surfaces studied, the surface structure changes dramatically with a small amount of gold. From the large size scan image of STM in Figure (4-2-2 (a)), we see that the larger terraces apparent on the clean surface break into smaller terraces. The terrace width of these small structures varies considerably.

It is also quite evident from the LEED image in (Figure 4-2-2 (b)) that the sharp spots evident on the clean surface are replaced by significant streaking along the $[11\bar{2}]$ direction.

a)

b)

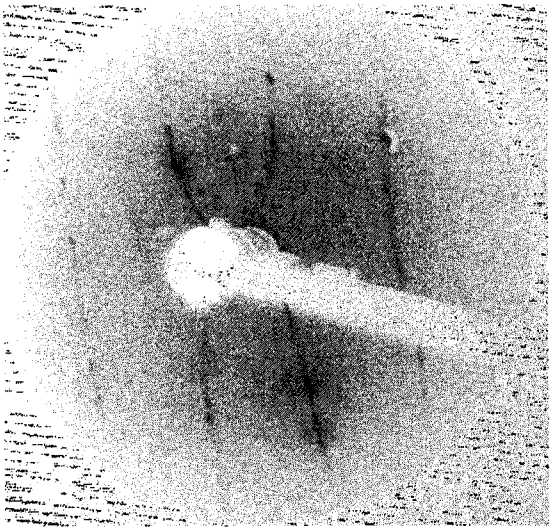

Figure 4-2-2 (a) An STM image (4630 Å ×4630 Å) of a 12.3° sample following 0.05±0.03 ML of Au. The image was taken at a bias of +2.3 V, and a current of 117 pA, with a PtRh tip. (b) Corresponding LEED image at energy of 72 eV.

At somewhat higher coverage (0.1ML) as in the Figure 4-2-3, the chain spacing becomes more regular. Large areas of the surface consist of uniform chains with a regular chain spacing of 36 Å. A 36 Å spacing corresponds to a Miller index of (13 13 7). This facet is tilted 14.4° towards $[11\bar{2}]$. From the STM image we see the (13 13 7) terraces are composed of regular chains with some bright protrusions. The large (13 13 7) terraces are separated occasionally by

atomic steps as indicated by arrows.

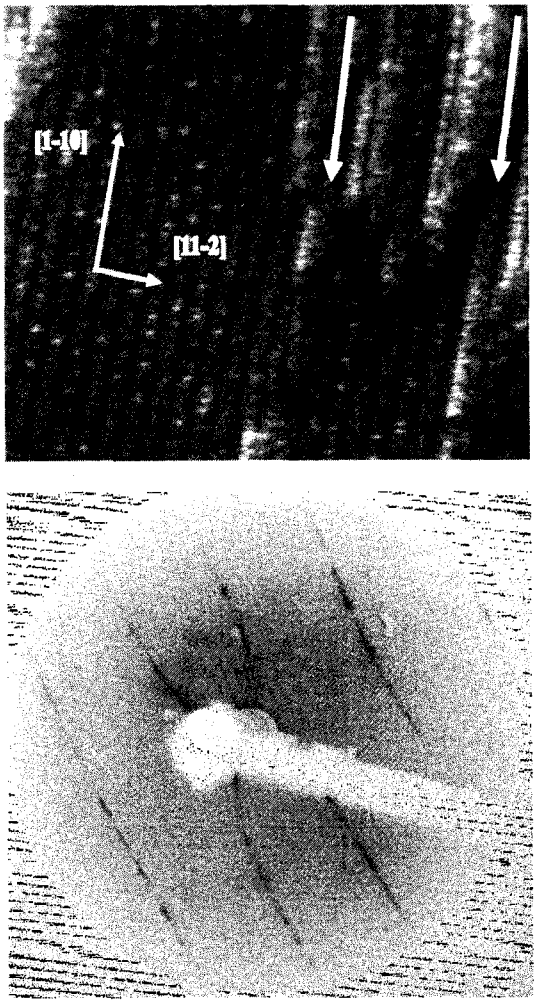

Figure 4-2-3 (a) An STM image (880 Å ×680 Å) of a 12.3° sample following 0.10±0.03 ML of Au deposition. The image was taken at a bias of -2.33 V, and a current of 320 pA, with a PtRh tip. Arrows indicate positions of atomic steps. (b) Corresponding LEED image taken at energy of 72 eV.

With more gold (0.13 ML), the periodicity of the 1-d structures is once again non-uniform (Figure 4-2-4). We observe at least three different chains structures in the STM image. One of the chain spacing is 41 Å, corresponding to a (13 13 11) facet, while another is 8 Å, corresponding to a (331) facet, and the third is 27 Å corresponding to a (997) facet. There are always two or three such structures coupled together. LEED exhibits spots running along $[11\,\bar{2}]$, with several

periodicities, consistent with STM.

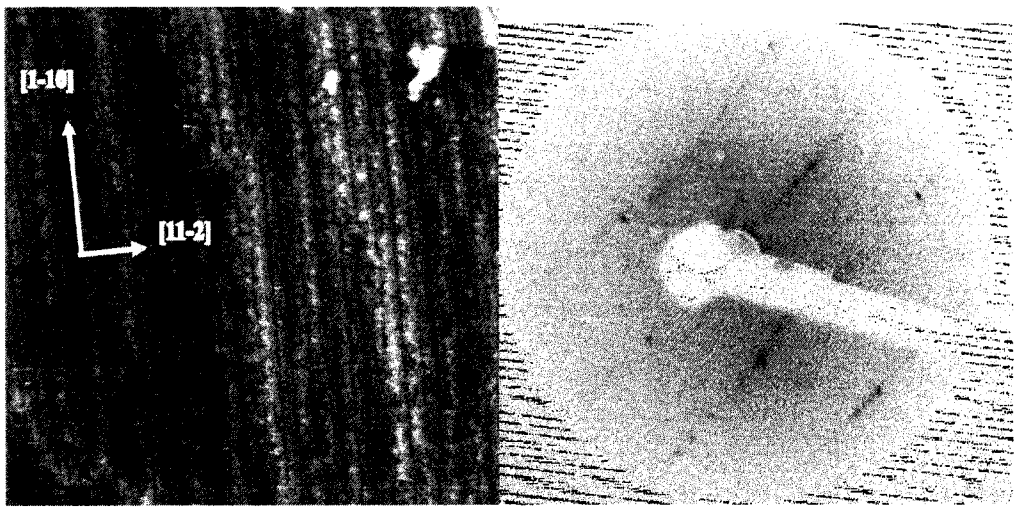

a) b)

Figure 4-2-4 (a) An STM image ($1000\,\mathring{A} \times 1000\,\mathring{A}$) of a 12.3° sample following 0.13±0.03 ML of Au. The image was taken at a bias of -2.3 V and a tunneling current of 0.88 nA with a PtRh tip. (b) Corresponding LEED image taken at energy of 72 eV.

Beyond 0.10 ML, we did not observe a surface with well-defined facets until a gold coverage of 0.20 ML. At 0.20 ML (Figure 4-2-5), we see large terraces separated by steps. On further investigation, Figure 4-2-5(b), we measured the chain spacing on the terraces and obtained a spacing of $25\,\mathring{A}$, corresponding to a (995) facet. LEED also reveals a sharp pattern with regular spaced spots along $[11\bar{2}]$ suggesting a regular chain spacing. From the LEED image we measure a chain spacing of $23\,\mathring{A}$ which is not inconsistent with the STM. In addition, we observe streaks in the LEED reminiscent of those in the Si(111)5x2 pattern which indicate periodicity along the chains.

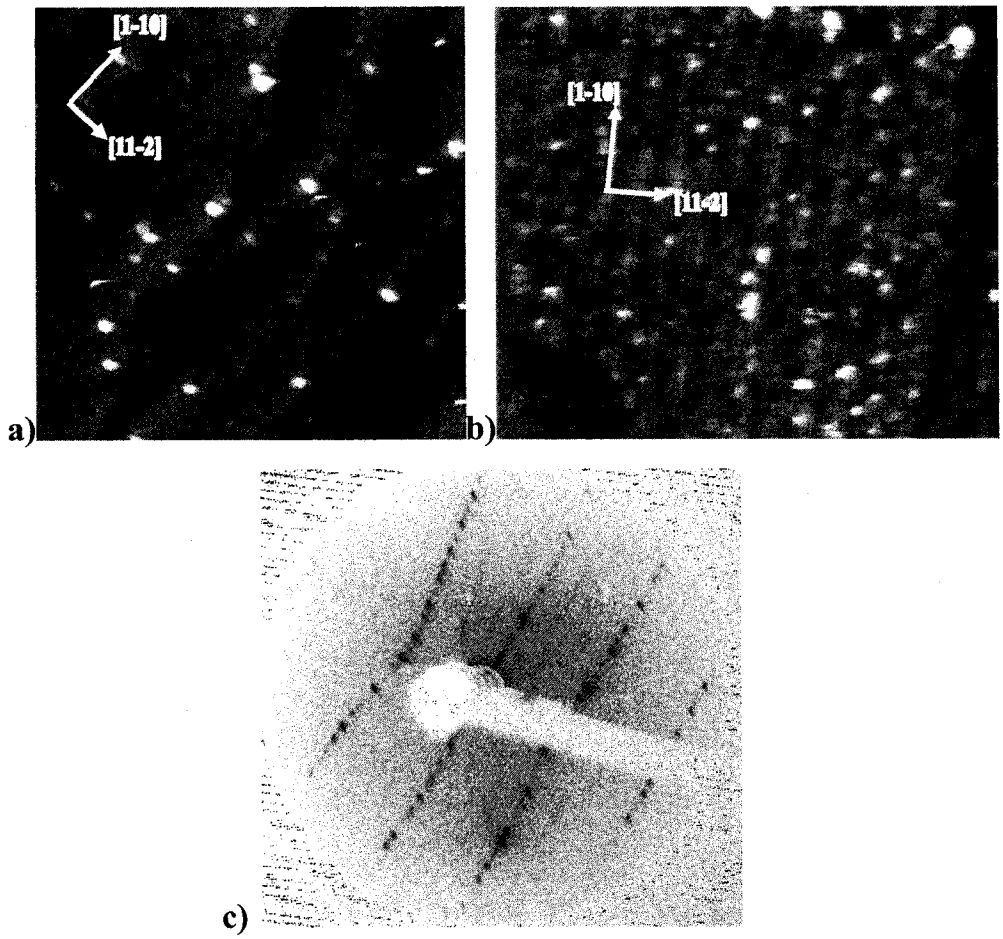

Figure 4-2-5 (a) An STM image (3280 Å ×3280 Å) of a 12.3° sample following 0.20±0.03 ML of Au. The image was taken at a bias of +2.4 V, and a tunnel current of 440 pA, with a PtRh tip. (b) An STM image (380 Å ×380 Å) of the same 12.3° sample. (c) Corresponding LEED image taken at energy of 72 eV.

At 0.24 ML, further restructuring takes place. The surface exhibits a well-ordered "hill-valley" structure. We can clearly see well defined facets as shown in Figure 4-2-6. From the line scan of (d) in the same figure it is evident that the relative angle between the facets is 5.9°. Since *a priori* we do not know the crystallographic orientation of either facet, to find the orientation of the surface we need to measure the chain spacing on one of the facets (Figure 4-2-6(b)). The measured chain spacing is 14.9 Å corresponds to a (553)-Au facet within

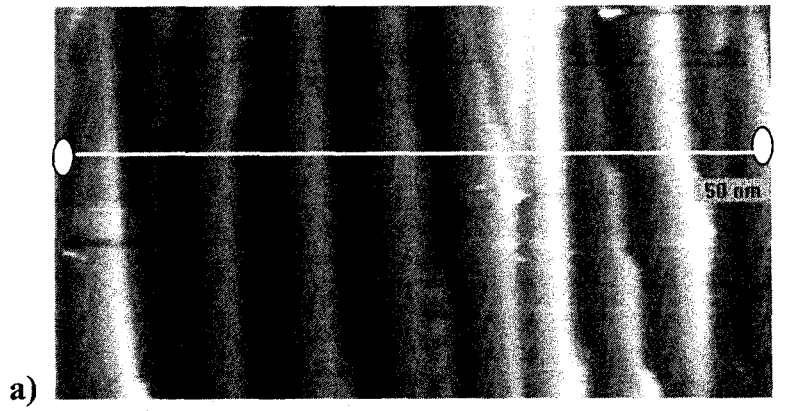

a)

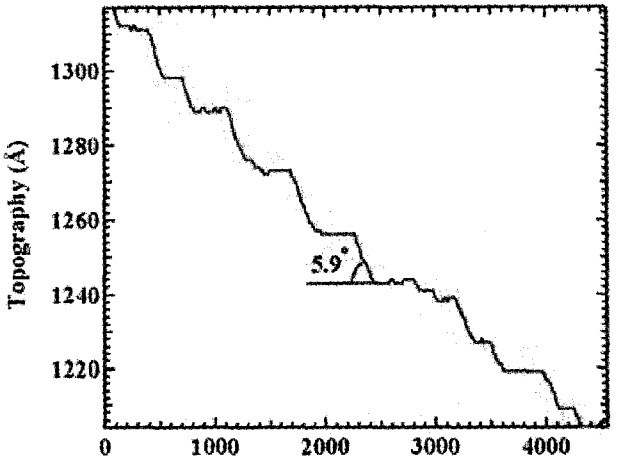

b)

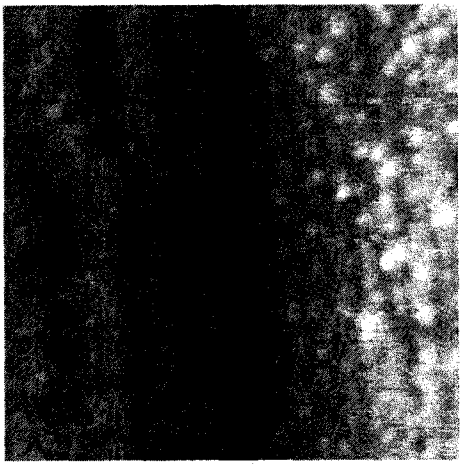

c)

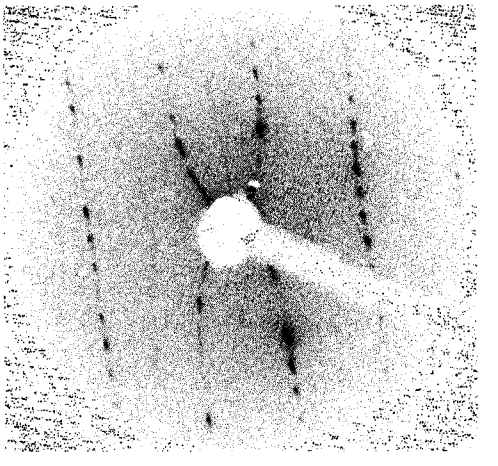

d)

Figure 4-2-6 (a) An STM image (2700 Å ×4500 Å) of a 12.3° sample following 0.24±0.03 ML of Au. The image was taken at a bias of -2.4 V, and a tunnel current of 320 nA, with a PtRh tip. (b) Corresponding line scan (c) An STM image (230 Å ×250 Å) of the same 12.3° sample. (d) Corresponding LEED image at energy of 72 eV.

error. The (553) facet is oriented 12.5° from (111). The measured chain spacing on the other facet is 28.1 Å, and corresponds to (997) facet which is oriented 6.6° away from the (111) plane. The difference between these two facets is 5.9° in agreement with the angle measured in Figure 4-2-6(a). The LEED image in part (c) of the same figure shows a sharp LEED pattern, exhibiting sharp regular spots running along $[11\bar{2}]$ indicating well formed facets consistent with STM.

Chapter 5: Discussion

In the previous chapter, we have presented our experimental results on the Au-induced morphology of samples miscut 3.8° and 12.3° towards [11$\bar{2}$]. As discussed in this thesis, several authors have investigated the Au-induced morphology of similar samples[23,26,29,31,33]. The common observation made by these groups was that at a certain gold coverage well-defined (775) facets are formed characterized by 1-d chains spaced 21.3 Å apart running along [1$\bar{1}$0]. It has been argued that the driving force for the formation of the (775) facet is the fact that the structure is closely related to Si(111)5x2-Au reconstruction. The 5x2 structure is the preferred Au–induced reconstruction on (111) terraces.

On both samples we find that the morphology is sensitive to gold deposition. Clearly gold deposition has a large effect on step-step interactions and mass transport. For example, 0.04 ML of gold changes the morphology of the 3.8° surface dramatically. The large flat terraces on the clean surfaces break up into smaller (111) terraces. On the 12.3° sample, 0.05 ML of gold is sufficient to break up the large uniform (995) facets and induce narrow terraces with a variety of chain spacings.

In agreement with others, we find the deposition of gold onto the 3.8° surface does induce formation of (775) facets, although it does not occur until 0.44 ML. This result is in contrast to the results of Shibata et al.[32] who observed well–defined (775) facets at a Au coverage of 0.31 ML on 4° samples deposited at 700°C. Hild et al.[33] observed the onset of (775) facets at 0.2 ML on similarly prepared samples with LEED. On 8° samples, Pedri et al.[35] observed the (775)

facet over a wide range of gold coverage (0.03-0.32 ML).

As mentioned, initial gold adsorption eliminates large terraces resulting in small terraces separated by atomic steps. With further gold deposition, the steps come together once again forming larger terraces separated by regions of step bunching. At 0.18 ML for example, the step bunching is sufficiently regular so that a facet with an inclination angle of 7.8° can be defined.

While the original gold does migrate exclusively to the step edges, at 0.20 ML we observe a 5x2 reconstruction on the large (111) terraces. The small (111) terraces associated with the step bunching still exhibit 7x7 reconstruction. This is consistent with O'Mahony et al.[26] who observed 5x2 regions on (111) terraces prior to the formation of (775) facets, however this is in contrast to the 8° experiments,[35] where gold migrates exclusively to the steps and the terraces remain gold free until 0.31 ML.

With more gold (0.31-0.43 ML), the steps become more regular and 1-d chains are observed. Initially a variety of chains structures are formed, however eventually the 21Å spacing dominates the entire facets. At this stage the (775) facet is fully developed and the surface is covered by alternating (775) facets and (111)5x2-Au terraces in agreement with Seehofer et al.[31]

Beyond 0.44 ML, in agreement with previous reports, the (775) facet is no longer observed. According to Pedri et al.[35] the stoichiometry of the (775)-Au facet corresponds to a local coverage of 0.24 ML. Similarly, the local coverage of 5x2 corresponds to 0.44 ML. Therefore beyond 0.44 ML, excess gold must be accommodated on the surface by steeper facets than (775). For example, at

0.46 ML the surface is composed of (553)-Au facets with a shorter chain spacing and (111)5x2-Au terraces.

In summary, our result on the 3.8° samples is consistent with the idea that the (775) facet is a low energy facet for surfaces miscut towards $[11\bar{2}]$. Since the sample miscut on the 8° sample is close to the orientation of (775) facets (8.5°), the (775) facet appears over a wide range of gold coverage. On the 3.8° sample, however, the formation of the (775) facet is more gradual, and the driving force for the surfaces to form (775) facets is not as strong. As a result, the gold induced 5x2 reconstruction appears on the flat terrace before the (775) facets are fully formed. The smaller driving force may also explain the slight differences that some groups observe for samples prepared under different conditions.

The evolution of the surface morphology of the 12.3° sample is quite different. 12.3° exceeds the 8.5° angle of the (775) facet. In all the cases we studied (0-0.24 ML), we did not observe any (775) facets on the surface. In all cases, the surface consists of 1-d structures running along $[1\bar{1}0]$. For example, the clean surface exhibits a uniform chain spacing of 26 Å. Based on the periodicity and the overall miscut angle of the wafer this corresponds to a (995) facet.

STM and LEED measurements indicate that gold adsorption induces the further formation of 1-d chain structures. With the exception of specific coverages discussed below, in general the surfaces exhibit a mixture of chain structures leading to a rather disordered surface morphology. At 0.10 ML however, the surface exhibits large terraces with a single well-defined chain spacing of 36 Å. From the chain spacing and the overall miscut of the wafer, we identify this as a

(13 13 7) facet which is tilted 14.4° towards $[11\bar{2}]$. Similarly at 0.20 ML, we observed a well defined chain spacing of 25 Å consistent with a (995) facet. Also a well-defined chain spacing of 14.6 Å was observed at 0.24 ML corresponding to a (553) facet. At this coverage the (553) facets were separated by (997) facets to preserve the overall miscut of the wafer.

Below saturation coverage, on the 3.8° and 8° samples the Au-induced (775) facet represents the low energy structure. On the 12.3° surface however, the stable facet depends on gold coverage. At 0.10 ML, 0.20 ML, and 0.24 ML, the surface forms (13 13 7), (995), (553) facets respectively. All three facets have a miscut angle close to 12.3°. With increasing gold coverage facets with shorter chain spacing become more stable, i.e. (13 13 7)→(995)→(553). At intermediate coverages the surface exhibits a mixture of chains associated with these facets.

Although we have not observed a (775) facet on the 12.3° sample up to 0.24 ML, it may occur at higher coverage. To preserve the miscut of the sample the (775) facet must be accompanied by a much steeper facet (steeper than 12.3°). The local coverage of the (775) facet is 0.24 ML, and the coverage of the steeper facet would have to be even higher. In other words, we would not expect to see the (775) facet in the range of coverage we have investigated.

Chapter 6: Conclusion

In this thesis, we have extended the previous work done in this lab on 8° samples to study the gold induced morphology of samples miscut 3.8° and 12.3° towards $[11\bar{2}]$. Using STM, LEED and AES techniques we have measured the morphology of surfaces over a coverage range of 0-0.46 ML on the 3.8° samples and up to 0.24 ML on the 12.3° samples. In agreement with others we find that gold adsorption has dramatic effects on surface structure. An extremely small amount of gold completely changes the step-step interactions and resultant terrace-step morphology.

On the 3.8° samples, gold adsorption led to the formation of well-defined (775) facets separated by (111)5x2-Au terraces. The (775) facets were not fully developed until 0.43 ML, and initial gold adsorption did not occur exclusively at the step edges. By comparison, on the 8° samples the (775) facet was observed at the onset of adsorption and gold migrates exclusively to step edges until 0.31 ML. Beyond 0.44 ML the surface exhibits steeper facets to accommodate more gold. Our results are consistent with the previous idea that the (775) facet represents a low energy facet on Au-induced samples miscut towards $[11\bar{2}]$.

For the 12.3° samples, we did not observe (775) facets in the 0-0.24 ML range we investigated. Rather than a single low energy facet, we observed three Au-induced facets with a miscut angle close to 12.3°. (13 13 7), (995), (553) facets are formed at 0.10 ML, 0.20 ML, and 0.24 ML respectively. The energy difference between these facets is small as evidenced by the fact that at intermediate coverages the surface is comprised of a mixture of chain structures

producing a disordered surface.

References

1. Xiaosheng Fang and Lide Zhang; "One-Dimensional (1D) ZnS nanomaterials and Nanostructures"; *Journal of Materials Science &Technology* **22** 06, 721-736. (2006).

2. F. Dell'Olio, V.M.N. Passaro and F. De, Leonardis; "A silicon-on-insulator photonic wire based evanescent field sensor"; IEEE Photon. Technol. Lett **8** 9, 2520 (2006).

3. J. Viernow, J-L. Lin, D.Y. Petrovykh, F.M. Leibsle, F.K. Men and F.J. Himpsel; "Regular step arrays on silicon"; *Applied Physics Letters* **72**, 948-950. (1998).

4. J.N. Crain, A. Kirakosian, K.N, Altmann, D. Bromberger, S.C. Erwin, J.L. McChesney, J.-L. Lin and F.J. Himpsel; "Fractional Band Filling in an Atomic Chain Structure"; *Physical Review Letters* **90**,176805 (2003).

5. F.J. Himpsel, A. Kirakosian, J.N. Crain, J-L. Lin and D.Y. Petrovykh; "Self-assembly of one-dimensional nanostructures at silicon surfaces"; *Solid State Communications* **117**, 149-157 (2001).

6. K.N. Altmann, J.N. Crain, A. Kirakosian, J.-L. Lin, D.Y. Petrovykh and F.J. Himpsel; "Electronic structure of atomic chains on vicinal Si(111)-Au"; *Physical Review B* **64**, 035406 (2001).

7. A.A, Baski, K.M. Saoud and K.M. Jones; "1-D nanostructures grown on the Si(5 5 12) surface"; *Applied Surface Science* **7150**, 1-7 (2001).

8. R. Losio, K.N. Altmann, J.-L. Lin, D.Y. Petrovykh and F.J. Himpsel; "Band Splitting for Si(557)-Au: Is It Spin-Charge Separation?" *Physical Review Letters* **86** 4632-4635 (2001).

9. J.L. McChesney, J.N. Crain, V. Perez-Dieste, F. Zheng, M.C. Gallagher, M. Bissen, C. Gundelach and F.J. Himpsel; "Electronic stabilization of a 5x4 dopant superlattice on Si(111)5x2-Au"; Physical Review B 70, 195430 (2004).

10. J.M. Luttinger; "An exactly soluble model of a many-fermion system"; *Journal of Mathematical Physics* **4** 1154-1162 (1963).

11. R.F. Peierls; *Quantum Theory of Solids*; Oxford University Press: London, (1955).

12. J.N. Crain and F.J. Himpsel; "Functionalization of silicon step arrays I: Au passivation of stepped Si (111) templates"; Journal of Applied Physics A 90 (7), 3286-3290 (2001).

13. Charles Kittel; *"Introduction to Solid State Physics, Seventh Edition";* John Wiley and Sons: Toronto, (1996).

14. K. Takayanagi, Y. Tanishiro, M. Takahashi and S. Takahashi; "Structural analysis of Si (111)7x7 by UHV-transmission electron diffraction and microscopy"; *Journal of vacuum science and technology A* **3**, 31502-1506 (1985).

15. Joseph, A. Stroscio and William, J. Kaiser; "Scanning Tunneling Microscopy"; Methods of Experimental Physics 27 Academic Press, Inc. London, (1993).

16. G. Binnig, H. Rohrer, C. Gerber and E. Weibel; "7x7 Reconstruction on Si (111) Resolved in Real Space"; *Physical Review Letters* **50**, 120-123 (1983).

17. D. J. Chadi; "Theoretical study of the atomic structure of silicon(211), (311), and (331) surfaces"; Physical Review B **29** (2), 785-792 (1984).

18. S. S. Kosolobov, S.A. Song, L.I. Fedina, A.K. Gutakovski and A.V. Latyshev; "Instability of the Distribution of Atomic Steps on Si(111) upon Submonolayer Gold Adsorption at High Temperatures"; *JETP Letters* **81** (3), 117–121 (2005).

19. B.S. Swartzentruber, Y-W. Mo, M.B. Webb and M.G. Lagally; "Scanning tunneling microscopy studies of structural disorder and steps on Si surfaces"; *J.Vac.Sci.Technol A* **7** (4), 2901-2905 (1989).

20. C. Schelling, G Springholz and F. Schäffler; "Kinetic Growth Instabilities on Vicinal Si(001) Surfaces"; *Physical Review Letters* **83** (5), 356-360 (1999).

21. J.L. Lin, D.Y. Petrovykh, J.Viemow, F.K. Men, D.J. Seo and F.J. Himpsel; "Formation of regular step arrays on Si(111)7x7"; Journal of Applied Physics **84** (1), 255-260 (1998).

22. I.R. Collins, J.T. Moran, P.T. Andrews, R. Cosso, J.D. O'Mahony, J.F. McGilp and G. Margaritondo; "Angle-resolved photoemission from an unusual quasi-one-dimensional metallic system: a single domain Au-induced 5x2 reconstruction of Si(111)"; *Surface Science* **325,** 45-49 (1995).

23. R. Losio, K.N. Altmann and F.J. Himpsel; "Continuous Transition from Two-to-One-Dimensional States in Si(111)-(5x2)-Au"; *Physical Review Letters* **85,** 808-811 (2000).

24. T. Hasegawa, S. Hosoki and K Yagi; "Stable phase boundaries between the 7x7 and the 5x2 Au structures on a Si(111) surfaces studied by high-temperature STM"; *Surface Science* **355,** L295-L299 (1996).

25. E. Bauer;"The Si(111)-(5x1) Au structure"; *Surface Science* **250**, L379-L382 (1991).

26. J. D. O'Mahony and J. F. McGilp; "Nucleation and evolution of the Au-induced 5x2 structure on vicinal Si (111)"; *Physical review B* **49** (4), 2527-2535 (1994).

27. Steven C. Erwin; "Self-Doping of Gold Chains on Silicon: A New Structural Model for Si(111)-(5x2)-Au"; *Physical Review Letters* **91** (20), 206101 (2003).

28. Y. Yabuuchi, F. Shoji, K. Oura and T. Hanawa; *Surf. Sci* **131,** L412. (1983).

29. Lonny D. Berman and Boris W. Batterman; "Structure of submonolayer gold on silicon(111) from x-ray standing-wave triangulation"; *Physical Review B* **38** (8), 5397-5405 (1988).

30. J.N. Crain, J.L. McChesney, Fan Zheng, M.C. Gallagher, P.C. Snijders, M. Bissen, C. Gundelach, S C. Erwin and F.J. Himpsel; "Chains of gold atoms with tailored electronics states"; *Physical Review B* **69**, 125401 (2004).

31. L. Seehofer, S.Huhs, F. Falkenberg and R.L. Johnson; "Gold-induced faceting of Si (111)"; *Surface Science* **329,** 157-166 (1995).

32 Motoshi Shibata, Isao Sumita and Masato Nakajima; "Scanning-tunneling-micoroscopy study of initial stages of Au adsorption on vicinal Si (111) surfaces"; *Physical Review B* **53** (7), 15 Februry (1996).

33. R. Hild, C Seifert, M. Kammler, F.-J. Meyer zu Heringdorf, M. Horn-von-Hoegen, R.A. Zhachuk and B.Z. Olshanetsky; "Kinetics of Au induced faceting of vicinal Si (111)"; *Surface Science*, **512,** 117-127. (2002).

34. M. Jalochowski, M. Strozak and R. Zdyb; "Gold-induced ordering on vicinal Si (111)"; Surface science **375**, 203-209, (1997).

35. Laura Pedri; "Gold induced Nanostructuring of Silicon Surfaces"; Department of Physics, M.Sc thesis, *Lakehead University*, Thunder Bay, (2005).

36. Koyu Aoki, Takayauki Suzuki, Hiroki Minoda, Yasumasa Tanishiro and Katsumichi Yagi; "Au adsorption induced and phase transition of facet planes on the Si[110] zone studied by UHV-REM"; *Surface Science* **408,** 101-111 (1998).

37. Sampsa Riikonen and Daniel Sanchez-Portal; "Ab initio study of the double row model of the Si(553)-Au reconstruction"; *Surface Science* **600**, 1201-1206 (2006).

38. D.P. Woodruff and T.A. Delchar; "Modern Techniques of Surface Science, Second Edition". *Cambridge University Press*, 1994.

39. Edwards Vacuum Company, Manor Royal, Crawley, West Sussex, RH10 9LW UK.

40. John F. O'Hanlon; "A user's Guide to Vacuum Technology, Second Edition"; *John Wiley and Sons: New York*, (1989).

41. Varian, Inc. Corporate Headquarters, 3120 Hansen Way Palo Alto, CA 94304-1030 USA.

42. SAES Getters S.p.A., Viale Italia 77, 20020 Lainate (Milan) – Italy.

43. C.J. Davisson and L.H. Germer, *Physical Review* **30**, 705 (1927).

44. OCI Vacuum Microengineering Inc., 340 Saskatoon St., London, Ontario N5W 4R3, Canada.

45. L. Toppozini; "The design, construction and calibration of an evaporator for submonolayer deposition of Au onto the Si(111) surface"; Department of Physics, Honours Thesis, Lakehead University, Thunder Bay, (2004).

46. C.C. Chang; "Auger Electron Spectroscopy". Surface Science **25**, 53-59 (1971).

47. Omicron NanoTechnology GmbH, Limburger Str. 75, 65232 Taunusstein, Germany.

48. C. Julian Chen; "Introduction to Scanning Tunneling Microscopy"; Oxford Series In Optical And Imaging Sciences. *Oxford University Press*, USA (1993).

49. J. Tersoff and D. R. Hamann; "Theory of the scanning tunneling microscope"; P*hysicalRreview B* **31** (2), 805-813 (1985).

50. J. Bardeen; "Tunneling from a many-particle point of view"; *Physical Review Letters* **6** (2), 57-59 (1961).

51. RHK Technology, 1050 East Maple Road, Troy, MI 48083 USA.

52. Y.N. Yang, Elain S. Fu and Ellen D. Williams; "An STM study of current-induced step bunching on Si(111)"; *Surface Science* **356** (1-3), 101-111 (1996).

53. Ircon, Inc., 7300 N. Natchez Avenue Niles, Illinois 60714 USA.

54 . R.J. Phaneuf, N.C. Bartelt and Ellen D.Williams; "Low-Energy Electron-Microscopy Investigations of Orientational Phase Separation on Vicinal Si (111) Surfaces"; *Physical review letters* **67** (21), 2986-2989 (1991).

55. R.J. Phaneuf, Ellen D.Williams and N.C. Bartelt; "Temperature dependence of vicinal Si (111) surfaces"; *Physical Review B* **38** (3), 1984-1993 (1988).

56. W. Swiech, E. Bauer and M. Mundschau; *Surf. Sci* **253**, 283 (1991).

57. J.N. Crain, M.C. Gallagher, J.L. McChesney, M. Bissen and F. J. Himpsel; "Doping of a surface band on Si(111)$\sqrt{3}$ Å $\times$ $\sqrt{3}$ Å-Ag"; *Physical Review B* **72**, 045312 (2005).